Graduate School Form 30
Updated 1/15/2015

PURDUE UNIVERSITY
GRADUATE SCHOOL
Thesis/Dissertation Acceptance

This is to certify that the thesis/dissertation prepared

By Akshay Gajanan Sane

Entitled

HIGH-FIDELITY MODELLING OF A BULLDOZER USING AN EXPLICIT MULTIBODY DYNAMICS FINITE ELEMENT CODE WITH INTEGRATED DISCRETE ELEMENT METHOD

For the degree of Master of Science in Mechanical Engineering

Is approved by the final examining committee:

Tamer Wasfy
Chair

Khosrow Nematollahi

Hazim El-Mounayri

To the best of my knowledge and as understood by the student in the Thesis/Dissertation Agreement, Publication Delay, and Certification Disclaimer (Graduate School Form 32), this thesis/dissertation adheres to the provisions of Purdue University's "Policy of Integrity in Research" and the use of copyright material.

Approved by Major Professor(s): Tamer Wasfy

Approved by: Sohel Anwar 4/16/2015

Head of the Departmental Graduate Program Date

www.manaraa.com

المنارة للاستشارات
www.manaraa.com

HIGH-FIDELITY MODELLING OF A BULLDOZER USING AN EXPLICIT MULTIBODY DYNAMICS FINITE ELEMENT CODE WITH INTEGRATED DISCRETE ELEMENT METHOD

A Thesis

Submitted to the Faculty

of

Purdue University

by

Akshay Gajanan Sane

In Partial Fulfillment of the

Requirements for the Degree

of

Master of Science in Mechanical Engineering

May 2015

Purdue University

Indianapolis, Indiana

www.manaraa.com

ProQuest Number: 1599090

All rights reserved

INFORMATION TO ALL USERS
The quality of this reproduction is dependent upon the quality of the copy submitted.

In the unlikely event that the author did not send a complete manuscript
and there are missing pages, these will be noted. Also, if material had to be removed,
a note will indicate the deletion.

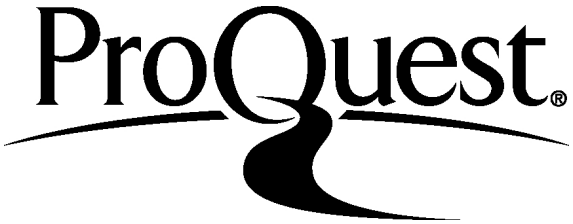

ProQuest 1599090

Published by ProQuest LLC (2015). Copyright of the Dissertation is held by the Author.

All rights reserved.
This work is protected against unauthorized copying under Title 17, United States Code
Microform Edition © ProQuest LLC.

ProQuest LLC.
789 East Eisenhower Parkway
P.O. Box 1346
Ann Arbor, MI 48106 - 1346

www.manaraa.com

ACKNOWLEDGMENTS

It would not have been possible to write this Master's thesis without the help and support of the several individuals who in one way or another contributed their valuable help and time in the completion of this study.

I would like to express my special thanks to Dr. Tamer Wasfy for providing me this opportunity to learn and gain this much experience throughout my study. Without his technical advice, support and patience, this work could not be done.

Also, I want to thank my advising committee, Dr. Hazim El-Mounayari and Dr. Nematollahi for their time and direction during the completion of this thesis.

I appreciate Mechanical Engineering Department faculty and staff for their instruction and advice through my graduate courses. I would also like to express my gratitude to Valerie Lim Diemer for her kindness in formatting this thesis.

I would like to thank my dear parents, brother, friends and my aunt for supporting and motivating me through all the stages of my life. I am very proud to have such kind people around me.

www.manaraa.com

TABLE OF CONTENTS

www.manaraa.com

LIST OF TABLES

www.manaraa.com

LIST OF FIGURES

www.manaraa.com

Figure Page

www.manaraa.com

Figure Page

www.manaraa.com

Figure Page

www.manaraa.com

ABSTRACT

Sane, Akshay Gajanan. M.S.M.E., Purdue University, May 2015. High-Fidelity Modelling of A Bulldozer Using An Explicit Multibody Dynamics Finite Element Code With Integrated Discrete Element Method. Major Professor: Tamer Wasfy.

In this thesis, an explicit time integration code which integrates multibody dynamics and the discrete element method is used for modelling the excavation and moving operation of cohesive soft soil (such as mud and snow) by bulldozers. A soft cohesive soil material model (that includes normal and tangential inter-particle force models) is used that can account for soil compressibility, plasticity, fracture, friction, viscosity and gain in cohesive strength due to compression. In addition, a time relaxation sub-model for the soil plastic deformation and cohesive strength is added in order to account for loss in soil cohesive strength and reduced bulk density due to tension or removal of the compression. This is essential in earth moving applications since the soil that is dug typically becomes loose soil that has lower shear strength and lower bulk density (larger volume) than compacted soil. If the model does not account for loss of soil shear strength then the dug soil pile in front of the blade of a bulldozer will have an artificially high shear strength. A penalty technique is used to impose joint and normal contact constraints. An asperity-based friction model is used to model contact and joint friction. A Cartesian Eulerian grid contact search algorithm is used to allow fast contact detection between particles. A recursive bounding box contact search algorithm is used to allow fast contact detection between the particles and polygonal contact surfaces.

A multibody dynamics bulldozer model is created which includes the chassis/body, C-frame, blade, wheels and hydraulic actuators. The components are modelled as rigid bodies and are connected using revolute and prismatic joints. Rotary actuators along with PD (Proportional-Derivative) controllers are used to drive the wheels.

www.manaraa.com

Linear actuators along with PD controllers are used to drive the hydraulic actuators. Polygonal contact surfaces are defined for the tires and blade to model the interaction between the soil and the bulldozer. Simulations of a bulldozer performing typical shallow digging operations in a cohesive soil are presented. The simulation of a rear wheel drive bulldozer shows that, it has a limited digging capacity compared to the 4-wheel drive bulldozer. The effect of the relaxation parameter can be easily observed from the variation in the Bulldozer's velocity. The higher the relaxation parameter, the higher is the bulldozer's velocity while it is crossing over the soil patch. For the low penetration depth run the bulldozer takes less time compared to high penetration depth. Also higher magnitudes of torques at front and rear wheels can be observed in case of high penetration depth. The model is used to predict the wheel torque, wheel speed, vehicle speed and actuator forces during shallow digging operations on three types of soils and at two blade penetration depths. The model presented can be used to predict the motion, loads and required actuators forces and to improve the design of the various bulldozer components such as the blade, tires, engine and hydraulic actuators.

www.manaraa.com

1. INTRODUCTION

1.1 Motivation

Bulldozers are typically used to perform earth moving operations such as excavation/digging (Figure 1.1), leveling, tilling, spreading earth, and backfilling trenches. They are used in many industries including: construction, mining, agricultural, forestry and military. In order to satisfy their customers and improve their market share, bulldozer manufacturers are spending substantial effort on research to improve the main bulldozer subsystems, including: drive engine, tracks, wheels, tires, blade, tiller, hydraulic actuators, and driver cabin. The main performance measures that customers require in bulldozers include:

- Long equipment life.
- Low operating costs. This includes: low fuel consumption (high energy efficiency) and low maintenance costs.
- High earth moving (digging, leveling, tilling, etc.) throughput.
- High operator safety.
- High operator comfort.

High fidelity multibody dynamic analysis can be used to optimize the design of bulldozers and their subsystems. Multibody dynamics can help with each of the above performance requirements. The following types of analyses can be performed using multibody dynamics software:

Prediction of dynamic stresses and internal forces during typical and extreme operating scenarios for the various bulldozer components such as tracks, sprockets, wheels, blades, hydraulic cylinders, various links, and joints/bearings. This can then

www.manaraa.com

Figure 1.1. Combined multibody dynamics/DEM model of a bulldozer performing an earth leveling operation on mud

be used to size the component, predict the component fatigue life, and optimize the components design (minimize weight and maximize durability). In addition, the fatigue life prediction can be used to schedule necessary maintenance activities such as inspection or replacement of components.

- *Prediction of the energy and power requirements* of the drive engine and hydraulic actuators in various operating scenarios such as moving/digging on soft soil and on level or sloped terrains.

- *Prediction of the digging throughput.* Multibody dynamics can be used to predict the effect of the various bulldozer design/operation parameters such as blade geometry, blade angle with respect to the soil, and drive motor torque on the digging throughput.

- *Prediction of the mobility and maximum speed* on various soils and terrains.

www.manaraa.com

- *Vibration analysis* can be performed using multibody dynamics. Operators comfort levels can be improved using the simulation results.

- *Prediction of bulldozer stability* on sloped soft and hard terrains during typical operating scenarios in order to avoid tipping over.

In all the above analyses accurate modelling of the interaction between the bulldozer and the soil is essential in order to obtain accurate predictions from the multibody dynamics model. In this thesis, a high-fidelity multibody dynamics model of a bulldozer is created using a commercial multibody dynamics code which also includes a discrete element granular soil modelling capability. The code is used to model the excavation and earth moving operation of cohesive soft soil (such as mud and snow) by bulldozers.

1.2 Literature Review

Literature reviews of rigid and flexible multibody dynamics modelling techniques were presented in Schiehlen [1] and Wasfy and Noor [2], respectively. The multibody dynamics formulation used in the present paper was presented in Refs. [3–19] and has the following characteristics:

- The procedure which is used is called explicit time-integration solution,which makes use of lumped mass/inertia tensor [3]. The solution cost per time step is directly proportional to the number of elements. The relation can be approximated as linear. These elements can be divided on available processor cores. These cores make use of a linear parallel speed-up thus making the solution procedure embarrassingly parallel. Internal force and torque vectors are evaluated using time averaged positions and velocities. A much larger explicit time step can be used after filtering out high-frequency modes.

- A body fixed frame is used to write the rotational equations of motion in which the body inertia tensor is constant. The rotation of the rigid bodies is measured

www.manaraa.com

by using the total rotation matrix relative to the inertial frame. The total body rotation matrix is updated using an incremental rotation matrix. These correspond to incremental rotation angles. The rotational equations of motion are integrated to obtain rotational angles [4]. The rigid-body rotations are referred to a body-fixed frame and all remaining solid solution fields are referred to the global inertial reference frame.

- Joint constraints include cylindrical, spherical, prismatic, and revolute joints. All these are modelled using penalty technique [4].
- Master/slave contact model where contact is identified between discrete points on a master contact surface and a polygonal slave contact surface [5–8].
- The contact penetration between points on the master contact surfaces and polygons on slave contact surfaces is discovered by utilizinig general fast binary-tree hierarchical bounding box/sphere contact search algorithm [5, 6].
- Penalty technique is used to impose the normal contact constraints [5–8].
- An accurate and numerically efficient asperity-based friction model is used to model the friction at contact surfaces and joints [9, 10].
- Total-Lagrangian lumped parameters 3D finite elements including spring/truss, thin shell [3], thin beam [11], thick beam [14], and solid finite elements [12, 13].
- Large complex vehicle models can be created using hierarchical object-oriented structure [15–19].

The simulation of soil which is considered as a granular media is still an undergoing research. Stability of material, especially during the simulations is the main focus in classical soil mechanics. Number of available numerical methods to simulate the operation of earth moving equipment has increased over the years. And they have become more efficient and faster due to advances in computational resources. Multi-core

www.manaraa.com

GPUs are used to perform the most complex calculations and simulations. Mechanically, soil can be roughly classified into non-cohesive soil (such as sand, silt or gravel), cohesive soft soil (such as mud, clay, and snow), and cemented/hard soil (such as asphalt, concrete, stone and rock) [20]. In this thesis we will focus on cohesive soft soil. Cohesive soft soil is composed of particles which vary in size, shape, density, damping, stiffness, strength, friction coefficient, moisture content and inter-particle attraction forces (such as chemical bonding forces, electro-static forces, capillary liquid-bridging forces and van der Waals forces). The particle size can vary from a few microns to a few millimeters. Modelling individual particles with a full scale bulldozer model requires using billions of particles. This is unachievable on existing highly configured computers. Therefore, current soil models that are suitable for use in coupled multibody dynamics soil problems such as bulldozer's earth moving simulations use particles modelled as lump terrain. These models define force models for soil to soil and soil to tire/track interactions. These are experimentally tuned to approximate physical response of the soil.

The simulation of soil mechanics is an active research area due to its applications in many engineering areas such as geotechnical engineering, vehicle mobility, and earth moving equipment design. Following are the techniques for modelling soft soils which are based on the type of lumping and model fidelity: (1) fully-lumped models; (2) phenomenological height field-based models; (3) finite element method; (4) particle models.

1.2.1 Fully Lumped Models

These models predict the steady-state traction and motion resistance on various types of soft terrains by utilizing experimentally tuned equations/algorithms. Above parameters are defined as a function of terrain conditions. Terrain conditions include soil depth, bulk density, soil type, soil cone index, soil moisture content, roughness, and slope. Vehicle parameters include vehicle weight, tire speed, tire width/diameter,

www.manaraa.com

etc. [21, 22]. These types of models were integrated in the vehicle modbility models presented in NRMM [23] and NRMM-II [24]. Although these models have been extensively used in the past to model vehicle-soil interaction, their range of validity is limited to the experimental conditions that they were calibrated on.

1.2.2 Phenomenological Height Field-Based Models

These are typically used to model soil forces on tires or tracks since they calculate the normal and tangential forces (between a tire or track and a plastically deformable soil surface) based on sinkage (normal penetration) and relative normal and tangential velocities [25–27]. The Mohr-Coulomb failure criteria is used to model soil shear failure. This criteria is parameterized by the soil cohesion and the angle of internal friction. Literature review shows that such models were integrated into DADS [28], ADAMS [29] and Recurdyn [30, 31] for modelling vehicle mobility on soft soils. In [32–34] a phenomenological terrain model was integrated into the SIMPACK [35] multibody dynamics code. The soil surface was described using a "digital elevation map" and the wheel contact surface was represented as a point cloud. A hierarchical bounding box algorithm was used to allow fast contact detection. An erosion algorithm was added to allow forming heaps in front of the wheels and side ruts. In [36] a phenomenological terrain was developed using a spring-damper tire model and a visco-elasto-plastic soil compressibility model. In this model each column of soil is divided into sub-volumes with each sub-volume having a loading state. Horizontal soil force/displacement produced by tractive and turning forces are incorporated into the model using the model proposed by Janosi and Hanamoto [37] which calculates the shear stress in terms of the shear displacement, normal stress, shear modulus, cohesion, and angle of internal friction. The main advantage of phenomenological terrain models is their computational speed. Their disadvantages include:

- These models are biased to the vertical direction since they use a vertical sinkage (height) field. This also makes them not suitable for modelling the digging

www.manaraa.com

operation of bulldozer blades since sinkage cannot be as clearly defined as in the case of tires and tracks.

- They do not account for the correct state of three dimensional deformation/stress in the soil.
- Ruts, heaps, and soil separation/reattachment effects are not accurately modelled.
- The range of validity of these models is generally limited to the cases they were tuned withh.

1.2.3 Finite Element Method

In this method soil deformation is modelled using the motion of the finite element nodes. This forms a Lagrangian finite element mesh [38–41] along with an elasto-visco-plastic constitutive material model such as DruckerPrager model [42]. This is used for modelling soil compaction and plastic deformation. The main drawback of this method is that it cannot simply model soil separation/reattachment and large soil deformation/flow (such as bulldozing and ruts). Modelling these effects requires remeshing and re-interpolating the solution field to the new mesh which is computationally expensive and considerably degrades the solution accuracy. In addition, the constitutive material models can approximately account for moderate material flow and cannot account for large material flow. Therefore, finite element soil models are typically suitable for modelling multibody soil interactions problems where the soil deformation is relatively small.

1.2.4 Particle Models

Discrete particles are used to model the soil with inter-particle forces. Such soil model represents the soil mechanical behaviour. Particle models are the closest models to the actual physics of the soil. The main drawback of particle models is the large

www.manaraa.com

number of particles and high computational cost required to accurately model the soil. Following are some of the popularly used particle based formulations that have been used to model soils: DEM (Discrete Element Method) [43–56], SPH (Smoothed Particle Hydrodynamics) [57–60], MPM (Material Point Method) [61–63] and PFEM (Particle Finite Element Method) [64,65]. Particle methods can easily handle surface break-up and merging and soil-solid impenetrability boundary condition.

In the Cundall et al. [43, 44] DEM inter-particle forces include: normal contact forces (which can be deflection and/or velocity dependent) which prevent the particles from penetrating each other, attraction forces, tangential contact forces (including friction and viscous forces) and distance dependent forces (gravity, electrostatic and magnetic forces). Particles can be either point particles or rigid body type particles. Particles can be of any arbitrary shape such as spherical, cubical, rod shaped etc. In Carrillo et al. [45] and Horner et al. [46] spherical particles were used with an inter-particle force model that included particle stiffness and friction but did not include cohesive (attractive) forces and plasticity. In Peters et al. [47], the DEM technique developed in [44, 45] was extended to non-spherical ellipsoid particles. A 2D DEM model that incorporates a tension spring for accounting the soil cohesion was developed for soil-tire interaction in Nakashima and Oida [48]. In Smith and Peng [49] the particle force model developed in [48] was implemented in a 3D DEM code. This model was used for modelling a rigid wheel interaction on a cohesive soil. In Negrut et al. [50,51] an implicit differential variational inequality (DVI) solver was developed for solving coupled DEM - multibody dynamics problems such as ground vehicles mobility and earth moving applications. In Tasora et al. [52] the DVI solver was extended to include a general particle force model that can account for soil plastic flow, cohesion and rolling friction. In this formulation, plastic flow must be stored in a fine eulerian mesh that covers the surface. This considerably increases the computational complexity and cost of the formulation. Rocks3D [53] is a proprietary DEM code developed at Caterpillar. This code is capable of modelling cohesive soils. It can link to Caterpillar proprietary multibody dynamics codes to perform coupled

www.manaraa.com

DEM multibody dynamics simulations, including various earth moving and vehicle mobility applications. In Ahmadi et al. [54] and Wasfy et al. [55] a DEM model was integrated into an explicit multibody dynamics code for modelling sand flow rate, angle of repose and a backhoe digging operation. Cubical rigid body particles were used with a force model that includes normal particle stiffness/damping, tangential viscous and Coulomb friction forces. In Wasfy et al. [56] a soft cohesive soil inter-particle force material model was added to the model developed in [53, 54]. This model accounts for soil compressibility, plasticity, friction, fracture, viscosity, cohesive strength and flow. The model was applied to the prediction vehicle mobility on soft soil.

SPH [57, 58] is a mesh-free method where the particles are used as interpolation points for solving the continuum mechanics governing equations (Cauchy equation of motion in the case of soils). The continuum equations are discretized for each particle using a kernel smoothing function that is used to evaluate each particle properties and fluxes/forces acting on a particle using neighboring particles. In [59,60] a coupled FEA/SPH model created in PAM-CRASH/PAM-SHOCK [66] is used to simulate the rolling rigid and flexible tires on a soft soil. A hydrodynamic elastic-plastic material was used for the soil. The SPH model showed promise but it was concluded that the material models need to be further refined since they either showed excessive viscosity or incorrect material compressibility.

In the MPM [61] a Cartesian grid is used along with the particles to find neighboring particles as well as to discretize and solve the continuum mechanics governing equations. In [62] the MPM was used to model snow for computer graphics applications. It included rigid body interaction, using a snow material model that includes stiffness, plasticity and fracture. In [63] MPM was used to model soil-structure interaction including pile driving and landslides using a non-linear hypo-elastic sand material model. In the PFEM developed in Idelsohn et al. [64] the particles are used to generate a polyhedral finite element mesh every time step using an extended Delaunay tessellation. The solution of the continuum mechanics governing equations is

www.manaraa.com

then carried using that mesh. The PFEM is used to model soil erosion and land-slides in Onate et al. [65]. Both the soil and fluid in the soil erosion problem were modelled using the PFEM. In [65] the PFEM was used to model sand type material flow from a hopper/silo, angle of repose and granular column collapse. Although this method may require less soil particles, however, the tessellation step needed every time step is computationally intensive and it can introduce modelling errors because of distorted elements.

SPH, MPM and PFEM rely on a continuum mechanics formulation. Most researchers conclude that more research is needed to develop a continuum mechanics constitutive material model that accurately accounts for material flow, plasticity, friction, fracture, compressibility, and cohesion. DEM naturally account for material flow. Also, DEM inter-particle force models that account for the rest of the above effects are easier to develop and are more robust than continuum mechanics constitutive models.

1.3 Thesis Objectives and Contributions

The objective of this thesis is to present a high-fidelity coupled multibody dynamics and discrete element model (DEM) of a bulldozer for predicting the earth moving operations of the bulldozer on cohesive soil such as mud and snow. A soft cohesive soil material model (that includes normal and tangential inter-particle force models) is used that can account for soil compressibility, plasticity, fracture, friction, viscosity, gain in cohesive strength due to compression, and loss in cohesive strength due to tension. A penalty technique is used to impose joint and normal contact constraints. An asperity-based friction model is used to model contact and joint friction. A Cartesian Eulerian grid contact search algorithm is used to allow fast contact detection between particles. A recursive bounding box contact search algorithm is used to allow fast contact detection between the particles and polygonal contact surfaces. Multibody dynamics software DIS (Dynamic Interactions Simulator) [67] developed by Advanced

www.manaraa.com

Science and Automation Corp. is used for creating the multibody dynamics model. The DIS code is an explicit time integration code with integrated DEM modelling capability. Thus, one solver is used for DEM, rigid multibody dynamics, and flexible (finite element) multibody dynamics.

The multibody dynamics bulldozer model includes the chassis/body, C-frame, blade, wheels, and hydraulic actuators. The components are modelled as rigid bodies and are connected using revolute and prismatic joints. Rotary actuators along with PD controllers are used to drive the wheels. Linear actuators along with PD controllers are used to model the hydraulic actuators. Polygonal contact surfaces are defined for the tires and blade to model the interaction between the soil and the bulldozer. Simulations of a bulldozer performing typical shallow digging operations on different types of cohesive soils and different blade penetration depths are presented. The model is used to predict the wheel torque, wheel speed, vehicle speed, and actuator forces during shallow digging operations on two types of soils and at two blade penetration depths. The model presented can be used to predict the loads and motion, and improve the design for the various bulldozer components such as the blade, tires, engine, and hydraulic actuators.

The main contributions of this thesis are:

- Creating of a high-fidelity coupled multibody dynamics DEM model for modelling the earth moving operations of bulldozers. The modelling techniques presented in [54–56] are applied to bulldozer earth moving applications.

- Adding to the soft cohesive soil material model developed in [56] an adhesion relaxation sub-model for the soil plastic deformation and cohesive strength, in order to account for loss in soil cohesive strength and reduced bulk density due to tension or removal of the compression. This is essential in earth moving applications since the soil that is dug typically becomes loose soil that has lower shear strength and lower bulk density (larger volume) than the original compacted soil. If the model does not account for loss of soil shear strength then

www.manaraa.com

the dug soil pile in front of the blade of a bulldozer will have an artificially high shear strength. The effect of the adhesion relaxation speed on the response of the bulldozer and soil is studied in this thesis using 3 models with three different adhesion relaxation speeds.

1.4 Thesis Organization

This thesis is organized as follows. In Chapter 2, the multibody dynamics formulation, including equations of motion, joints constraints, actuators and explicit solution procedure is briefly described. In Chapter 3, the multibody dynamics contact model and the DEM particle cohesive soil contact force model are presented. In this Chapter we propose some material tests to tune the cohesive soil contact force model. In addition, in Chapter 3 the contact search and detection algorithms are presented. In Chapter 4, the bulldozer multibody dynamics model is presented. In Chapter 5 typical simulations of shallow digging operations on cohesive soils are presented. Finally, concluding remarks are offered in Chapter 6.

www.manaraa.com

2. MULTIBODY DYNAMICS FORMULATION

2.1 Equations of Motion

The subsequent equations use the following conventions:

- Indicial notation.
- Einstein summation convention for repeated lower case subscript indices, unless otherwise noted.
- Upper case subscript indices denote node numbers.
- Lower case subscript indices denote vector component numbers.
- The superscript denotes time.
- A superposed dot denotes a time derivative.

Point particle nodes (which are used to model the soil particles) and rigid body nodes (which are used to model the vehicle rigid components) are the two types of finite element nodes which are used. rigid body nodes are charecterized of 3 translational and 3 rotational DOFs, where as the oint particle nodes have 3 translational DOFs (degrees of freedom). A modelling of a rigid boy is done by placing a finite element node at the rigid body's center of mass. In this algorithm, an explicit finite element code was presented for writing and integrating the equations of motion for spatial rigid bodies [4]. Global inertial reference frame is used to refer translational DOFs. Rotation matrix of each rigid body is also defined with respect to the global inertial frame. The singularity problems associated with parameter 3 are avoided when a total body rotation matrix to measure rigid body rotation avoids. Also issues with parameter 4 involving the measurements of Euler angles and Euler parameters. The

www.manaraa.com

translational equations of motion for the nodes are written with respect to the global inertial reference frame and are obtained by assembling the individual node equations. The equations can be written as:

$$M_K \ddot{x}^t_{Ki} = (F^t_s)_{Ki} + (F^t_a)_{Ki} \tag{1}$$

where t is the running time, K is the global node number (no summation over K; K = 1→N where N is the total number of nodes), i is the coordinate number (i = 1,2,3), M_K is the lumped mass of node K, x is the vector of nodal Cartesian coordinates with respect to the global inertial reference frame, and $\ddot{x}$ is the vector of nodal accelerations with respect to the global inertial reference frame, F_s is the vector of internal structural forces, and F_a is the vector of externally applied forces, which include surface forces and body forces.

For each rigid body (node), a body-fixed material frame is defined. The origin of the body frame is located at the body's center of mass. The mass of the body is concentrated at the center of mass and the inertia of the body is given by the inertia tensor I_{ij} defined with respect to the body frame. The orientation of the body frame is given by R^{to}_K which is the rotation matrix relative to the global inertial frame at time t_0. The rotational equations of motions are written for each node with respect to its body fixed material frame as:

$$I_{K_{ij}} \ddot{\theta}^t_{K_j} = (T^t_s)_{Ki} + (T^t_a)_{Ki} - \varepsilon_{ijk} \dot{\theta}^t_{K_j} (I_{K_{kq}} \dot{\theta}^t_{K_q}) \tag{2}$$

where $I_{K_{ij}}$ is the inertia tensor of rigid body K, $\ddot{\theta}^t_{K_j}$ and $\dot{\theta}^t_{K_j}$ are the angular acceleration and velocity vectors components for rigid body K relative to its material frame in direction j (j = 1,2,3), T_{sKi} and T_{aKi} are the components of the vector of internal and applied torques at node K in direction i of the local body frame and ε_{ijk} is the permutation tensor (to perform a cross product). Since, the rigid body rotational equations of motion are written in a body (material) frame, the inertia

www.manaraa.com

tensor $I_{K_{ij}}$ is constant. The trapezoidal rule is used as the time integration formula for solving Eq. (1) for the global nodal positions x:

$$\dot{x}^t_{K_j} = \dot{x}^{t-\Delta t}_{K_j} + 0.5\Delta t(\ddot{x}^t_{K_j} + \ddot{x}^{t-\Delta t}_{K_j}) \tag{3a}$$

$$x^t_{K_j} = x^{t-\Delta t}_{K_j} + 0.5\Delta t(\dot{x}^t_{K_j} + \dot{x}^{t-\Delta t}_{K_j}) \tag{3b}$$

Where Δt is the time step. The trapezoidal rule is also used as the time integration formula for the nodal rotation increments $\Delta\theta$:

$$\dot{\theta}^t_{K_j} = \dot{\theta}^{t-\Delta t}_{K_j} + 0.5\Delta t(\ddot{\theta}^t_{K_j} + \ddot{\theta}^{t-\Delta t}_{K_j}) \tag{4a}$$

$$\Delta\theta^t_{K_j} = 0.5\Delta t(\dot{\theta}^t_{K_j} + \dot{\theta}^{t-\Delta t}_{K_j}) \tag{4b}$$

Where $\Delta\theta_{K_j}$ are the incremental rotation angles around the three local frame axes for body K. Thus, the rotational equations of motion are integrated to yield the incremental rotations angles. The rotation matrix of body K (R_K) is updated using the rotation matrix corresponding to the incremental rotations angles:

$$R^t_{K_{ij}} = R^{t-\Delta t}_{K_{ik}}(R(\Delta\theta^t_{Kq}))_{kj} \tag{5}$$

Where $R(\Delta\theta^t_{Ki})$ is the rotation matrix corresponding to the incremental rotation angles from Eq. (4b). The structural force and torque vectors F_{sKi} and T_{sKi} can be a function of the position vector ($x^t_{K_j}$), velocity vector ($\dot{x}^t_{K_j}$), body rotation matrix ($R^t_{K_{ij}}$), and angular velocity vector ($\dot{\theta}^t_{K_j}$). However, rather than using the current values, the corresponding time averaged values ($x^t_{K_j}$, $\dot{x}^t_{K_j}$, $R^t_{K_{ij}}$ and $\dot{\theta}^t_{K_j}$) are used. This filters outs high-frequency modes and allows using a time step which is larger than the explicit time step depending on the value of the filtering factor. The average values are calculated as follows:

$$(x_a)^t_{Kj} = (1-\kappa)x^t_{Kj} + \kappa(x_a)^{t-\Delta t}_{Kj} \tag{6a}$$

$$(\dot{x}_a)^t_{Kj} = (1-\kappa)\dot{x}^t_{Kj} + \kappa(\dot{x}_a)^{t-\Delta t}_{Kj} \tag{6b}$$

$$(\dot{\theta}_a)^t_{Kj} = (1-\kappa)\dot{\theta}^t_{Kj} + \kappa(\dot{\theta}_a)^{t-\Delta t}_{Kj} \tag{6c}$$

www.manaraa.com

$$(\theta_a)^t_{Kj} = \Delta t(\dot{\theta}_a)^t_{Kj} \tag{6d}$$

$$(R_a)^t_{K_{ij}} = (R_a)^{t-\Delta t}_{K_{ik}}(R(\Delta(\theta_a)^t_{Kq}))_{kj} \tag{6e}$$

where κ is an averaging factor typically chosen between 0 to 0.9 (0 means no averaging and 0.9 means 90% averaging). Typically for $\kappa = 0.8$ the explicit time step can be increased by a factor of about 5.

The explicit solution procedure used for solving Eqs. (1-6) along with constraint equations is presented in Chapter 4. The constraint equations are generally algebraic equations, which describe the position or velocity of some of the nodes. They include:

- Joint constraints:

$$f(x) = 0 \tag{7}$$

- Contact constraints:

$$f(x) \geq 0 \tag{8}$$

- Prescribed motion constraints:

$$f(x,t) = 0 \tag{9}$$

2.2 Joint Constrains

Joint constraints are imposed using a penalty formulation. A joint imposes motion constraints between points on two bodies. The global position (x_{Gp}) and velocity ($\dot{x}_{Gp}$) of a point are given by (Figure 2.1):

$$(x_{Gp})_i = X_{B_i} + R_{B_{ij}}(x_{Lp})_j \tag{10a}$$

$$(\dot{x}_{Gp})_i = \dot{X}_{B_i} + R_{B_{ij}}(\vec{\dot{\theta}}_{BF} * \vec{x}_{Lp})_j \tag{10b}$$

where X_{B_i} and $\dot{X}_{B_i}$ are the global position and velocity vectors of the rigid body's frame, is the rotation matrix of the rigid body relative to the global reference frame, is the rigid body's angular velocity vector relative to its local frame, and x_{Lp} is the position of the point relative to the rigid body's frame.

www.manaraa.com

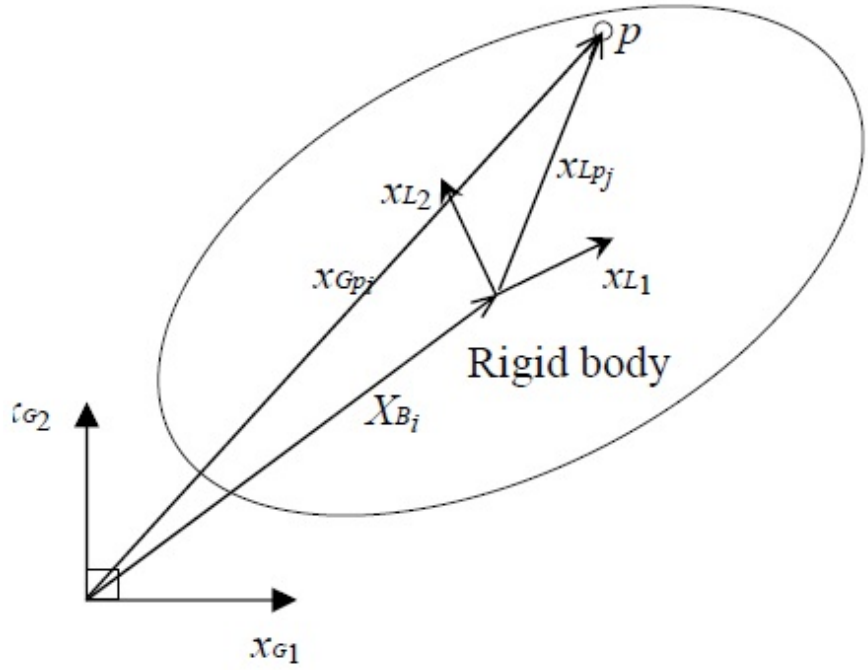

Figure 2.1. Location of a point on a rigid body with respect to the local body frame (x_{Lp}) and the global reference frame (x_{Gp}).

A joint is defined by specifying the relation between points on two bodies [4]. For example, a spherical joint (Figure 2.2) between two points is defined as:

$$(x_{Gc1})_i^t = (x_{Gc2})_i^t \tag{11}$$

Where $(x_{Gc1})_i^t$ the global position of the first point on the first body and $(x_{Gc2})_i^t$ is the global position of the second point on the second body. A spherical joint leaves 3 relative rotational DOFs (degrees-of-freedom) between the two rigid bodies free and constrains 3 relative translational DOFs. This constraint is imposed using the penalty technique as:

$$F_c = k_p d + c_p \dot{d}_i d_i / d \tag{12}$$

$$d_i = (x_{Gc1})_i^t - (x_{Gc2})_i^t \tag{13}$$

www.manaraa.com

$$\dot{d}_i = (\dot{x}_{Gc1})_i^t - (\dot{x}_{Gc2})_i^t \tag{14}$$

$$d = \sqrt{d_1^2 + d_2^2 + d_3^2} \tag{15}$$

$$F_{ci} = F_c d_i / d \tag{16}$$

where F_{ci} is the penalty reaction force on the connection point, k_p is the penalty spring stiffness, c_p is the penalty damping, d_i is the relative displacement vector between points c1 and c2, and $\dot{d}_i$ is the relative velocity vector between points c1 and c2. The constraint force is applied on the two connection points in opposite directions. Revolute joints can be modelled by placing two spherical joints along a line. Other types of joints such as prismatic, cylindrical, universal, planar, and screw joints can also be modelled by writing the constraint equation, then writing the corresponding penalty forces and moments for the connection points.

The constraint force F_{ci} is transferred to the node at the center of the body as a force and a moment using:

$$F_i = F_{ci} \tag{17a}$$

$$T_i = (x_{Lpi} * R_{BF_{ji}} F_{ci}) \tag{17b}$$

where

$$x_{Lpj} = R_{BF_{ji}}(x_{Gpi} - X_{BF_i}) \tag{18}$$

where F_i is the reaction force at the CG of rigid body 1 (center of the body frame), T_i is the reaction torque on rigid body 1, x_{Lcp} is the position of the contact point relative to the rigid body's frame and x_{Gcp} is the position of the contact point relative to the global reference frame. The force acting on rigid body 2 is equal and opposite to the force acting on rigid body 1. Thus, the negative of F_{ci} is transferred to the center of the connected rigid body 2 as a force and moment. The constraint forces given by Eq. (17a) are assembled into the global structural forces F_s in Eq. (1). The constraint torques given by Eqs. (17b) are assembled into the global structural torques T_s in Eq. (2).

Primitive spherical joints can be used to model various types of joints [4]. A revolute joint is modelled by placing two spherical joints along a line (Figure 2.3).

www.manaraa.com

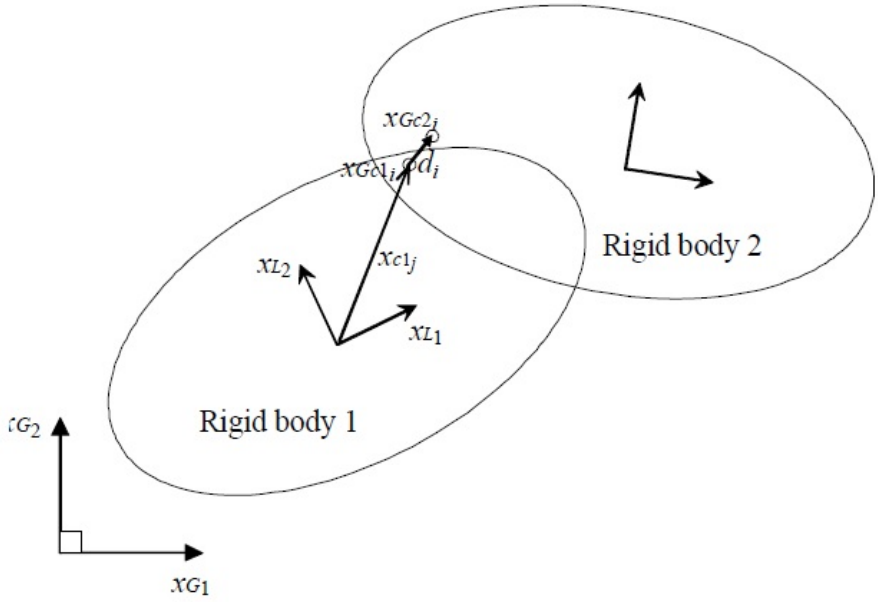

Figure 2.2. Spherical joint connecting two rigid bodies making two points x_{Gc1i} and x_{Gc2i} coincident.

A bracket joint is modelled using 3 or 4 non-coincident spherical joints between two rigid bodies. A cylindrical joint restricts a point on one body to move along a curve on another body [4] [68] (Figure 2.4). A prismatic joint can be modelled by placing two cylindrical joints in parallel.

2.3 Actuators

A linear actuator connects two points on two bodies (Figure 2.5). Using a PD controller, the force F is generated by the actuator is given by:

$$F = k(l - l_{des}) + c(\dot{l}_i l_i / l - \dot{l}_d es) \tag{19}$$

$$l_i = (x_{Gc1})_i^t - (x_{Gc2})_i^t \tag{20}$$

$$\dot{l}_i = (\dot{x}_{Gc1})_i^t - (\dot{x}_{Gc2})_i^t \tag{21}$$

$$l = \sqrt{l_1^2 + l_2^2 + l_3^2} \tag{22}$$

www.manaraa.com

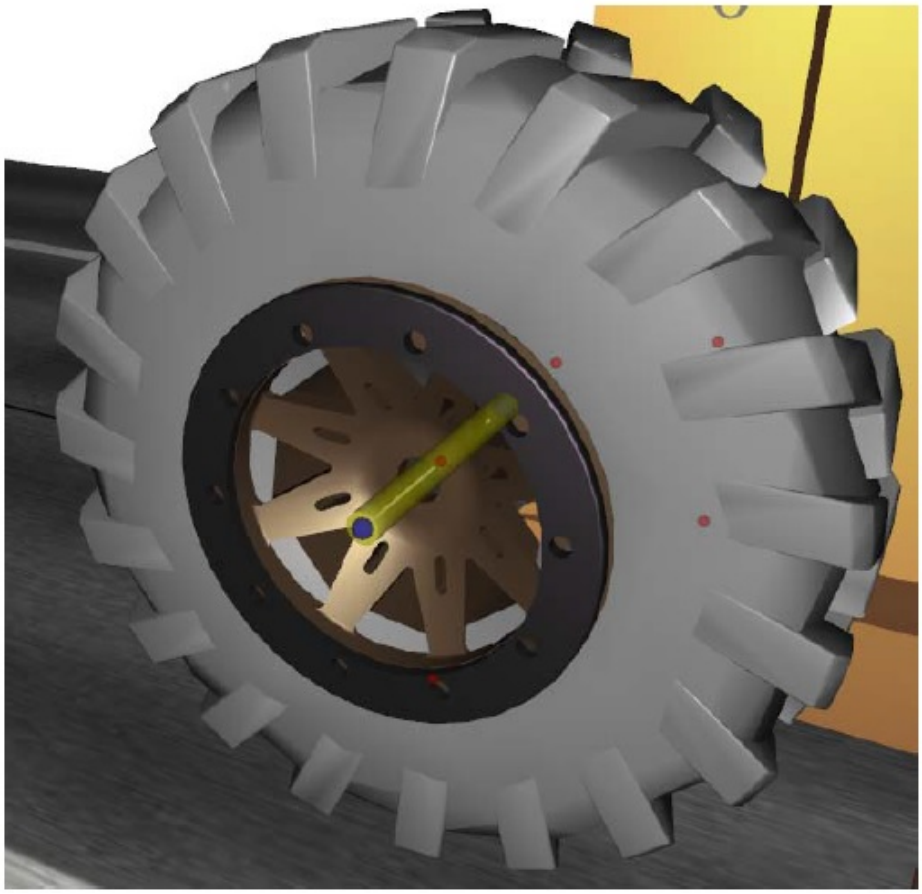

Figure 2.3. Revolute joint shown as a yellow cylinder is modelled using two spherical joints shown as blue spheres used to model the bulldozer wheel revolute joints.

$$F_i = Fl_i/l \tag{23}$$

where $(x_{Gc1})_i^t$ is the position of the first point on the first body and $(x_{Gc2})_i^t$ is the position of the second point on the second body, both with respect to the global reference frame; k is the controller proportional gain, c is the controller derivative gain, l_{des} is the desired length of the actuator, l is the current length of the actuator, and F_i is the actuator force vector. The actuator force is transferred to the rigid bodies center as a force and moment using Equations (17a) and (17b).

www.manaraa.com

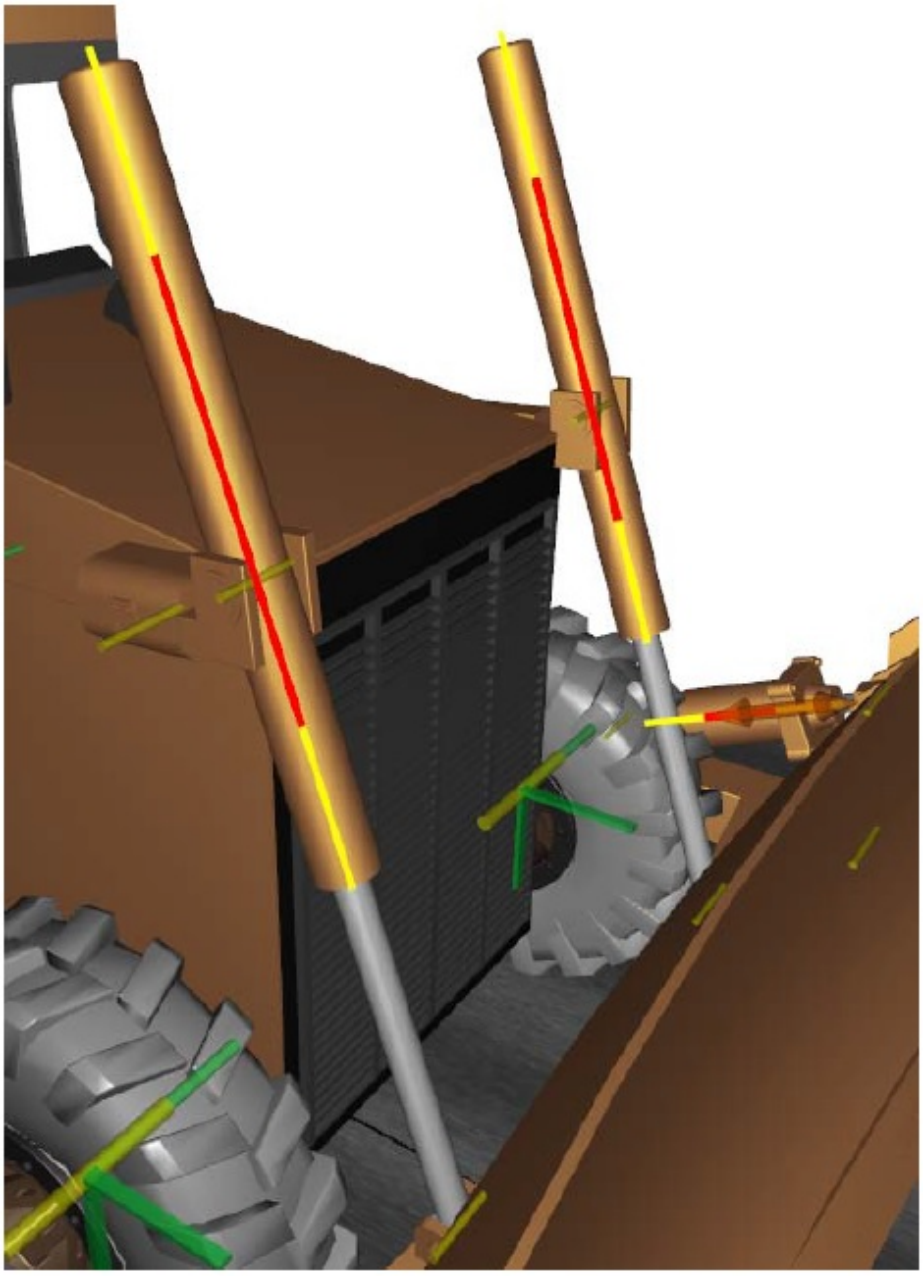

Figure 2.4. Cylindrical joints with the joint path shown as yellow line and the slider shown as a red line for modelling the bulldozers upper hydraulic actuators.

A rotational actuator connects three points on two bodies (Figure 2.6). Two of the points are on one rigid body and the third point is on the second rigid body. A PD controller is used for the actuator to generate torque T. It is given by:

$$T = k(\theta - \theta_{des}) + c(\dot{\theta} - \dot{\theta}_{des}) \tag{24}$$

www.manaraa.com

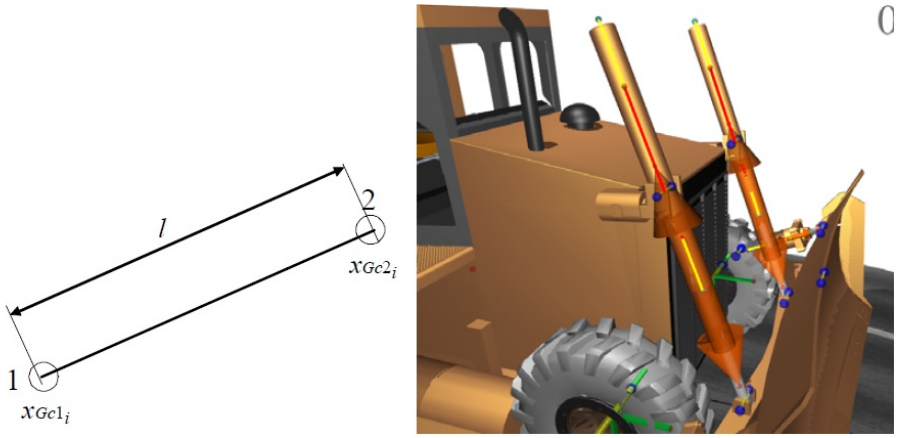

Figure 2.5. Linear actuator connecting two points (left). Linear hydraulic actuators shown as an orange cylinder with cones at both ends connecting a point on the cylinder to a point on the piston for the bulldozer upper hydraulic actuators (right).

where θ is the current angle of the actuator, θ_{des} is the desired angle, k is the proportional gain and c is the derivative gain. The rotary spring forces are transferred to the rigid bodies centers as force and moment using Equations (17a) and (17b). Rotational actuators are placed at the 4 wheels of the bulldozer in order to provide propulsion.

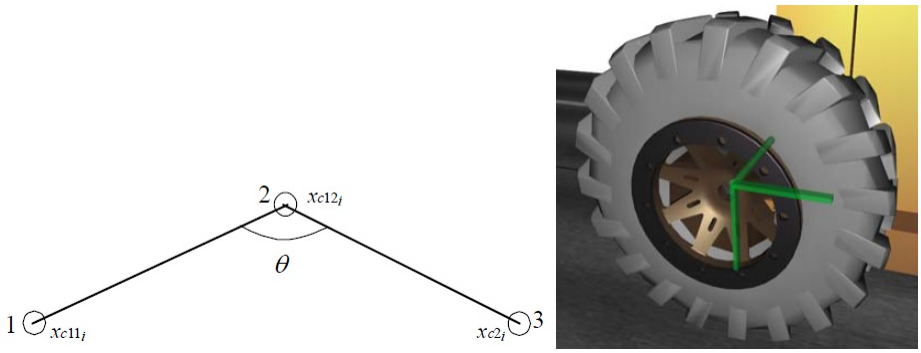

Figure 2.6. Rotational actuator connecting three points (lef). Rotational actuator for a bulldozer wheel shown as green cylinder which shows the axis of rotation and two green rectangular boxes showing two arms of actuator (right).

www.manaraa.com

2.4 Explicit Solution Procedure

The solution fields for modelling multibody systems are defined at the model nodes. Note that a rigid body is modelled as one finite element node. These solutions fields include: translational positions, velocities, and accelerations vectors; rotation matrices; and rotational velocities and accelerations vectors.

This solution procedure predicts the time evolution of the above response quantities. The main advantage of these solution procedures is that they are "embarrassingly" parallel. The procedure described below achieves near linear speed-up with the number of processors on shared memory parallel computers. The procedure was presented in [54] [55] [56] and is implemented in the DIS [67] (Dynamic Interactions Simulator) software code. The procedure is outlined below:

1-Prepare the run:

a. Set the initial conditions for the solution fields identified above.

b. Create a list of all the finite elements (Those also include joints and master contact surfaces which are considered to be elements).

c. Create a list of elements that will run on each processor. This is done using an algorithm which tries to make the computational cost on each processor equal.

d. Create a list of all the prescribed motion constraints.

e. Calculate the solid masses for each finite element node by looping through the list of finite elements. Note that the masses are fixed in time.

f. Loop over all the elements and find the minimum time step for the explicit solution procedure.

2-Loop over the solution time and increment the time by t each step while doing the following:

a. Set the nodal values at the last time step to be equal to the current nodal values for all solution fields.

b. Do 2 iterations (a predictor iteration and a corrector iteration) of the following:

www.manaraa.com

i. Initialize the nodal forces and moments to zero.

ii. Perform the inter-particle contact search algorithm (Section 3.2.1).

iii. Calculate the nodal forces and moments by looping through all the elements (and joints) while calculating and assembling the element nodal forces. This is the most computational intensive step. This step is done in parallel by running each list of elements identified in step 1.c on one processor.

iv. Find the nodal values at the current time step using the semi-discrete equations of motion and the trapezoidal time integration rule (Eqns. 1 - 5).

v. Find the average field values (Eqns. 6a - 6e).

vi. Execute the prescribed motion constraints which set the nodal value(s) to prescribed values.

vii. Go to the beginning of step 2.

www.manaraa.com

3. CONTACT MODEL

Contact is modelled between a contact point on a rigid body/particle (master body) and a surface on another rigid body/particle (slave body) [5] [6] [7] [8] (Figure 3.1). After contact is detected then the contact point on the slave contact surface is found. The position and velocity of the contact points are given by equations (10a) and (10b) respectively. The contact force at a contact point F_{c_i} is transferred to the center of the body as a force and a moment using equations (17a) and (17b) and the negative of the contact force is transferred to the contacting (slave) body. The contact force F_{c_i} can be divided into a normal force (F_{n_i}) and a tangential force (F_{t_i}):

$$F_{c_i} = F_{n_i} + F_{t_i} \tag{25}$$

The normal contact force vector is given by (Figure 3.1):

$$F_{n_i} = n_i |F_n| \tag{26}$$

Where n_i is the surface normal unit vector and $|F_n|$ is the signed magnitude of the normal force. The tangential contact force vector (F_{t_i}) is given by (Figure 3.1):

$$F_{t_i} = t_i |F_t| \tag{27}$$

Where:

$$v_{rel_i} = (\dot{x}_{Gc1})_i^t - (\dot{x}_{Gc2})_i^t \tag{28}$$

$$\Delta x_i = (x_{Gc1})_i^t - (x_{Gc2})_i^t \tag{29}$$

$$d = \sqrt{\Delta x_i \Delta x_i} \tag{30}$$

$$\dot{d} = v_{rel_i} n_i \tag{31}$$

www.manaraa.com

$$t_i = v_{t_i}/|\vec{v_t}| \tag{32}$$

$$v_{n_i} = \dot{d}n_i \tag{33}$$

$$v_{t_i} = v_{rel_i} - v_{n_i} \tag{34}$$

where t_i is a unit vector along the tangential contact direction, Δx_i is the relative position of the two contact points, v_{rel_i} is the relative velocity of the two contact points, d is the distance between the two contact points (closest distance between the contact point and the contact surface), $\dot{d}$ is the signed velocity in the direction of the normal to the contact surface, v_{n_i} is the relative normal velocity between the two contact points, and v_{t_i} is the relative tangential velocity between the two contact points.

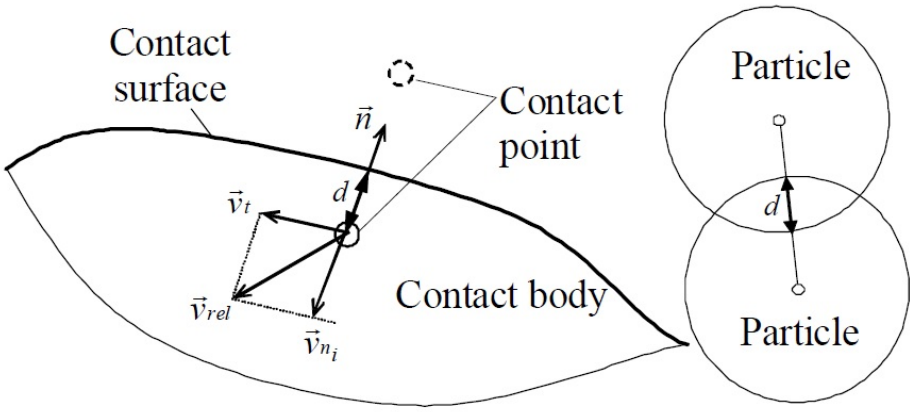

Figure 3.1. Contact surface and contact point and particle to particle contact. d is the penetration.

3.1 Cohesive Soil Force Model

In this section we will derive expressions for the normal force $|F_n|$ and tangential force $|F_t|$ to model cohesive soils and soil contact with vehicle surfaces (such as tires, wheels and track segments). This model was presented in Wasfy et al. [56]. $|F_n|$ is calculated using:

$$|F_n| = F_{adhesion} + F_{repulsion} + F_{damping} \tag{35}$$

www.manaraa.com

$F_{adhesion}$ and $F_{repulsion}$ are both specified as a function of contact point penetration into the contact surface d (Figure 3.2). Up to a penetration distance d_0 the contact forces are attractive thus joining the two bodies/particles together. A force greater than $F_{adhesion,max}$ is required to detach the two bodies. If the penetration goes beyond d_0 then the contact forces become repulsive thus opposing further penetration. The adhesion forces along with the friction forces contribute to the cohesive strength of the soil. Note that the adhesion and the repulsion force can be a non-linear function of the penetration distance. Thus, the shape of the curve in Figure 3.2 can be tuned using experimental data.

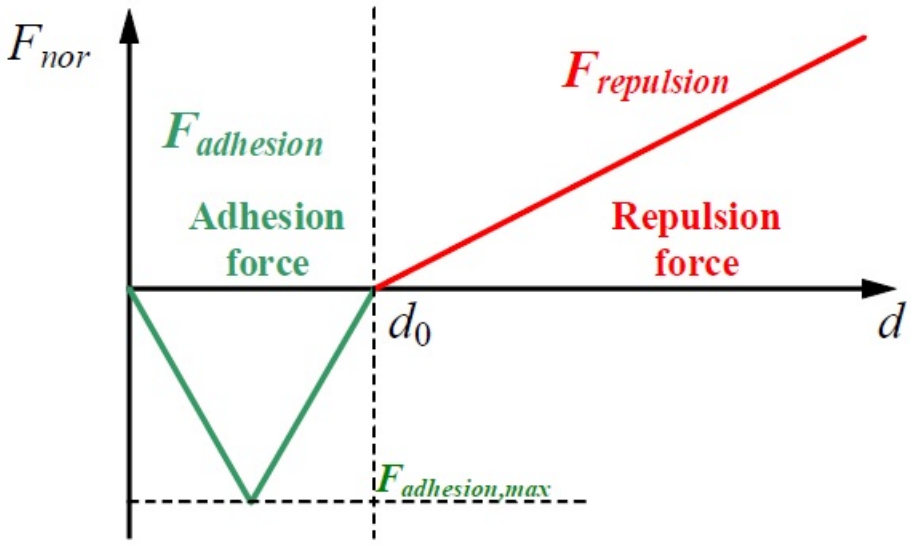

Figure 3.2. Normal adhesion and repulsion contact forces [56].

The normal damping force ($F_{damping}$) is given by:

$$F_{damping} = \begin{cases} c_n \dot{d}, & \dot{d} \geq 0 \\ s_n c_n \dot{d}, & \dot{d} < 0 \end{cases} \tag{36}$$

Where c_n is the damping coefficient and s_n is a separation damping factor (typically between 0 and 1) which reduces normal damping when the two bodies are moving apart. c_n can be specified as a function of d and $\dot{d}$.

www.manaraa.com

$|F_t|$is calculated using:

$$|F_t| = F_{viscous} + F_{friction} \tag{37}$$

The viscous force $F_{viscous}$ is given by:

$$F_{viscous} = c_t|v_t| \tag{38}$$

Where:

$$|v_t| = \sqrt{v_{t_i} v_{t_i}} \tag{39}$$

c_t is the viscosity coefficient and $|v_t|$ is the signed tangential velocity magnitude.

An asperity friction model is used along with the normal repulsion ($F_{repulsion}$) force to calculate the tangential friction force ($F_{friction}$) [9]. In this model, friction is modelled using a piece-wise linear velocity-dependent approximate Coulomb friction element in parallel with a variable anchor point spring. The model approximates asperity friction where friction forces between two rough surfaces in contact arise due to the interaction of the surface asperities (Figure 3.3).

When two surfaces are in static (stick) contact, the surface asperities act like tangential springs. When a tangential force is applied, the springs elastically deform and pull the surfaces to their original position. If the tangential force is large enough, the surface asperities yield (i.e. the springs break) allowing sliding to occur between the two surfaces. The separation force is proportional to the normal repulsion contact force ($F_{repulsion}$). In addition, when the two surfaces are sliding past each other, the asperities provide resistance to the motion. This resistance is a function of the sliding velocity and acceleration and the normal repulsion contact force. Figure 3.4 shows a schematic diagram of the asperity friction model. This model is composed of a simple piece-wise linear velocity-dependent approximate Coulomb friction element in parallel with a variable anchor point spring.

An asperity spring is used to connect two points on two bodies, but the model must keep track of which rigid bodies are in contact. It must consider the local position vectors of the asperity spring anchor points on the two contacting bodies. It

www.manaraa.com

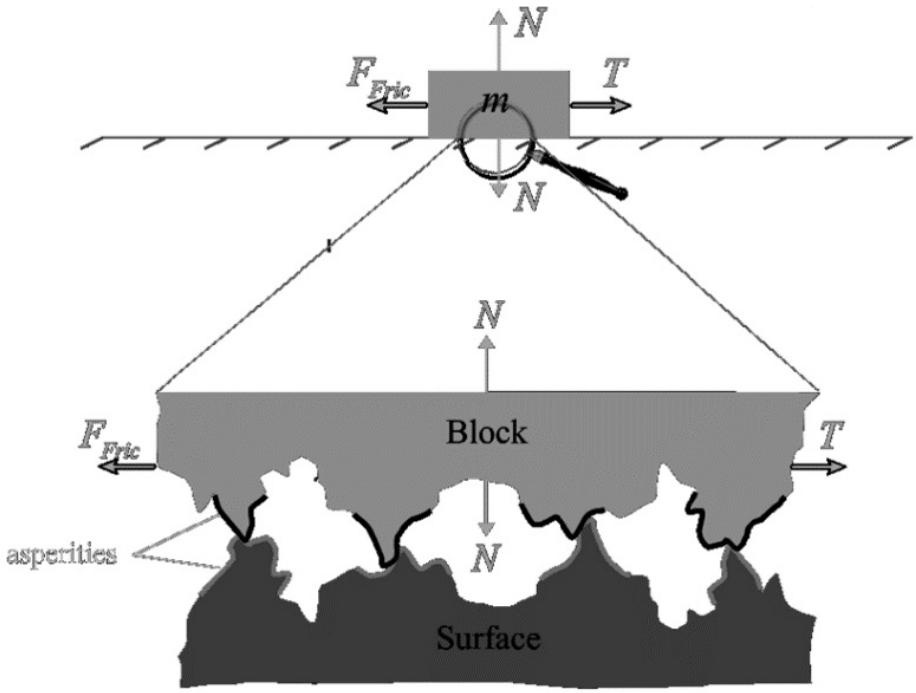

Figure 3.3. Asperity-based physical interpretation of friction [9].

is possible that the two rigid bodies can be in contact at more than one point, thus the model must keep track of the corresponding contact points on the two contact bodies.

To model the permanent plastic deformation of the soil, plastic deformation ($\delta_{plastic}$) can be specified as a function of repulsion (compression) force ($F_{repulsion}$) (e.g. Figure 3.5). The plastic deformation is subtracted from the particle radius. The $\delta_{plastic}$ versus $F_{repulsion}$ curve can be tuned to match the bulk density versus consolidating pressure curve for the soil (e.g. Figure 3.6) which specifies the plastic compressibility of the soil.

The increase in soil cohesive strength after consolidation can be taken into consideration by specifying the maximum adhesion force ($F_{adhesion,max}$) as a function of the plastic deformation (e.g. Figure 3.7). Also, the friction coefficient (μ), viscosity coefficient (c_n) and damping coefficient (c_t) can be specified as a function of the plastic deformation ($\delta_{plastic}$). The curve in Figure 3.8 along with the friction coefficient

www.manaraa.com

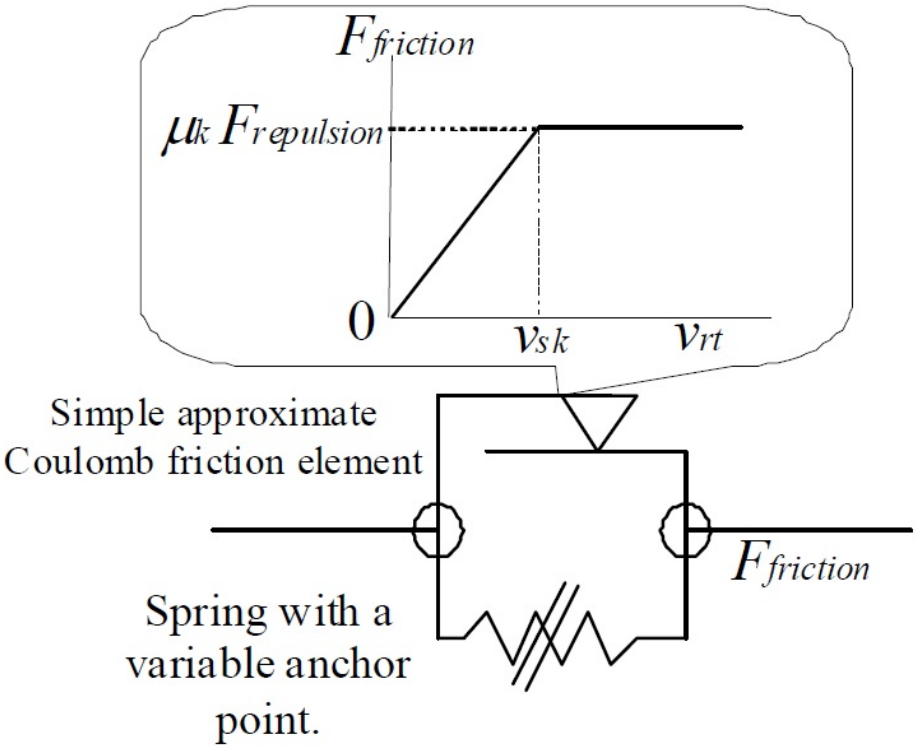

Figure 3.4. Asperity spring friction model. $F_{friction}$ Tangential friction force, $F_{repulsion}$ Normal repulsion force, μ_k Kinetic friction coefficient and v_{rt} Relative tangential velocity between two points in contact [9].

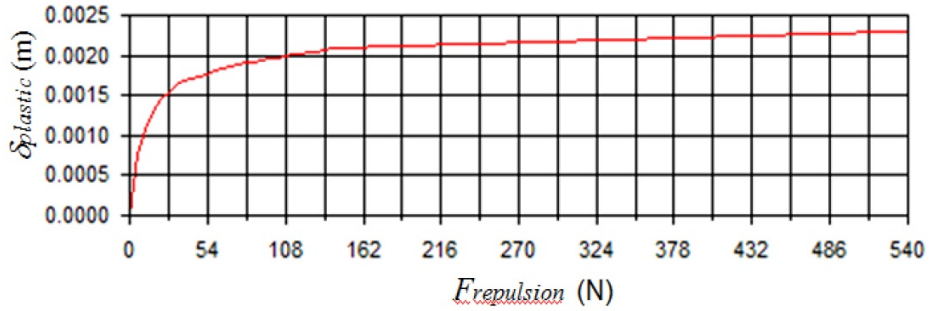

Figure 3.5. Typical curve of plastic deformation as a function of repulsion force [56].

can be tuned to match the shear stress versus normal stress for different pre-shear (consolidation) normal stress values [69]. An example of a typical shear stress versus

www.manaraa.com

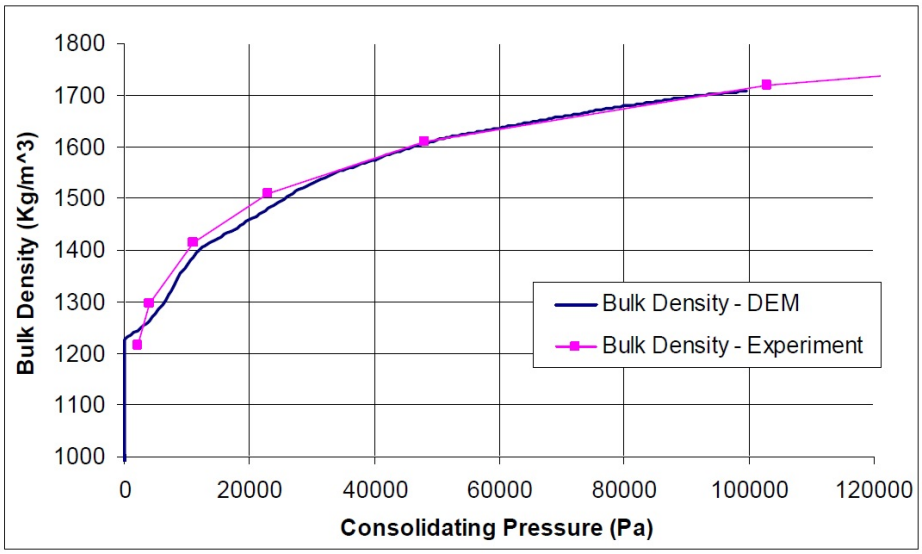

Figure 3.6. Typical bulk density versus normal pressure curve for a cohesive soft soil - comparison of experiment data and DEM model [56].

normal stress curve for one value of pre-shear (consolidation) normal stress is shown (Figure 3.8).

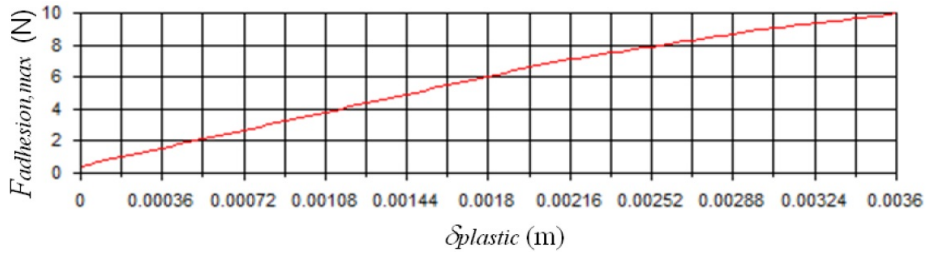

Figure 3.7. Typical adhesion force as function of plastic deformation [56].

In order to account for the reduction of soil cohesive strength and soil bulk density due to tension and/or removal of the compression, a time relaxation is applied to the soil plastic deformation each time step such that the plastic deformation of a particle ($\delta_{plastic}$) is given by:

www.manaraa.com

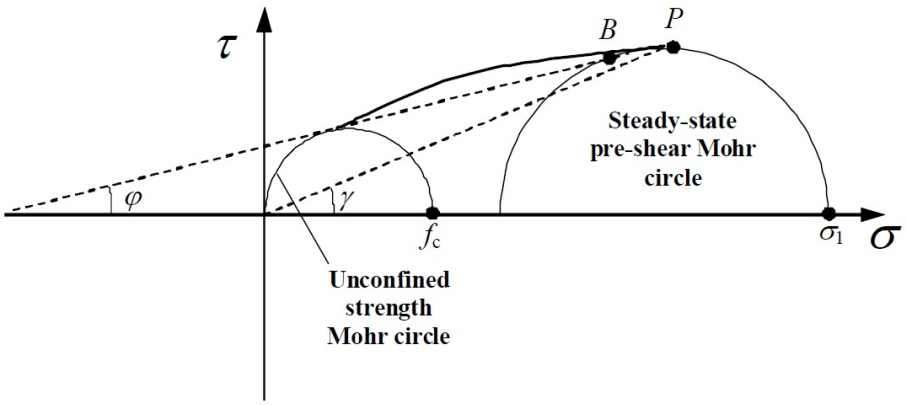

Figure 3.8. Yield locii and Mohr circles. P is the preshear point, f_c is the unconfined yield strength, σ_1 is the major consolidating stress, φ is the angle of internal friction, and γ is the effective angle of friction [69].

$$\delta_{plastic} = \delta_{plastic} - \begin{cases} 0, & F_{repulsion,max} \geq F_{adhesion,max} \\ V_{relax} * \Delta t, & F_{repulsion,max} < F_{adhesion,max} \end{cases} \tag{40}$$

Where V_{relax} is the speed of plastic/adhesion relaxation (in distance/time) and Δt is the explicit solution time step. Thus, if the particle maximum repulsion (compression) force is larger than the maximum adhesion (tension) force then the particle plastic deformation is left unchanged. If the particle maximum repulsion force is smaller than the maximum adhesion force then the particle plastic deformation is reduced at a speed of V_{relax}. The plastic deformation smallest allowable value is zero. The value of V_{relax} must be experimentally tuned. Since the plastic deformation is directly related (proportional) to the adhesion force using the graph in Figure 3.7, therefore reducing (relaxing) the plastic deformation also reduces the adhesion force and thus reduces the soil shear strength. Reducing the plastic deformation also reduces the bulk density of the soil (i.e. increases the volume of the soil).

The force model presented in this section can be used as the inter-particle force model for soft cohesive soils. The force model can be tuned to a particular soil material using the following experiments:

www.manaraa.com

- Piston - cylinder cell for measuring the soil bulk density versus consolidating pressure (Figures 3.5 and 3.6).
- Shear cell for measuring the soil cohesive strength and internal friction as a function of consolidation pressure and applied normal pressure (Figures 3.7 and 3.8).
- Penetrometer can also be used to tune the soil cohesive strength and inter-particle friction coefficient. However, the consolidation pressure and applied normal pressure cannot be applied independently. This makes this experiment only suitable for model verification.
- Angle of repose of a material pile can be used to tune the unconsolidated (loose) soil cohesive strength and inter-particle friction coefficient.
- Flow rate from hoppers can be used to tune the soil cohesive strength, inter-particle friction coefficient and wall adhesion.
- Wall material shear cell can be used to tune the friction and adhesion to wall materials.
- Blade soil experiments measuring the blade speed, drawbar force, normal force and sinkage. This experiment can be used to tune/verify the soil cohesive strength, inter-particle friction coefficient and plastic relaxation speed.
- Wheel soil experiments measuring torque, angular velocity, speed, drawbar force, normal force and sinkage. This experiment can be used to verify/tune the soil cohesive strength and inter-particle friction coefficient.

This force model can also be used as the particle-wall force model, since it can model the contact between the particle and other solid bodies. The force model can be tuned to particular soil and wall materials using a shear cell for measuring wall friction. It is possible that the particles can be point type particles (i.e. they have only translational DOFs and no rotational DOFs) or rigid body type particles (with

www.manaraa.com

both translational and rotational DOFs). The shape of the particles is a sphere in case of point particles whereas rigid body particles can have any arbitrary shape (see Section 3.2).

3.2 Contact Point Search

Contact detection is performed between contact points on the master contact surface of a rigid body and the slave contact surface on another rigid body. The slave contact surface can be: a superquadric surface (Figure 3.9), a collection of "glued" primitive shapes (including spheres Figure 3.10, cubes, ellipsoids, elliptical cylinders, Cones, Torii and superquadrics) or a polygonal surface (Figure 3.11) [54].

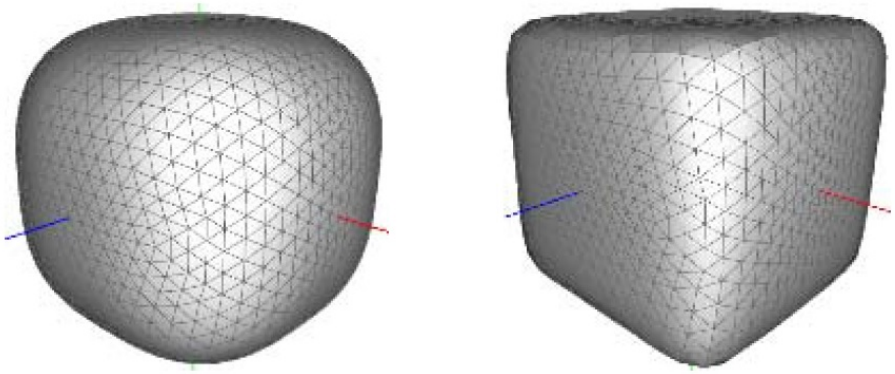

Figure 3.9. Particle of cubical shape modelled using superquadric with N = 3 (left) and N = 8 (right) [54].

If the slave contact surface is a polygonal surface (Figure 3.11), then a binary tree contact search algorithm [5] [6] [54] is used to detect the contact between a contact point of the master surface and polygons of the slave surface. Following steps are performed at the initialization of the algorithm:

- Each slave polygonal contact surface is divided into 2 blocks of polygons. The bounding box for each block of polygons is found. Then each of those blocks of polygons is divided into 2 blocks and again the bounding boxes for those blocks

www.manaraa.com

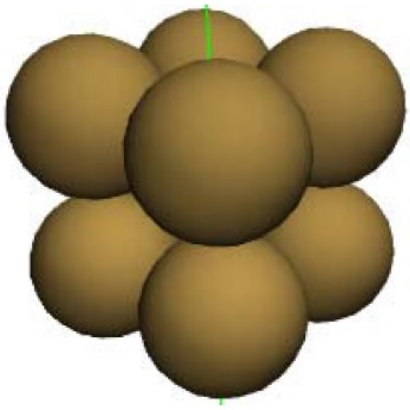

Figure 3.10. Particle of cubical shape modelled using 8 glued spheres [54].

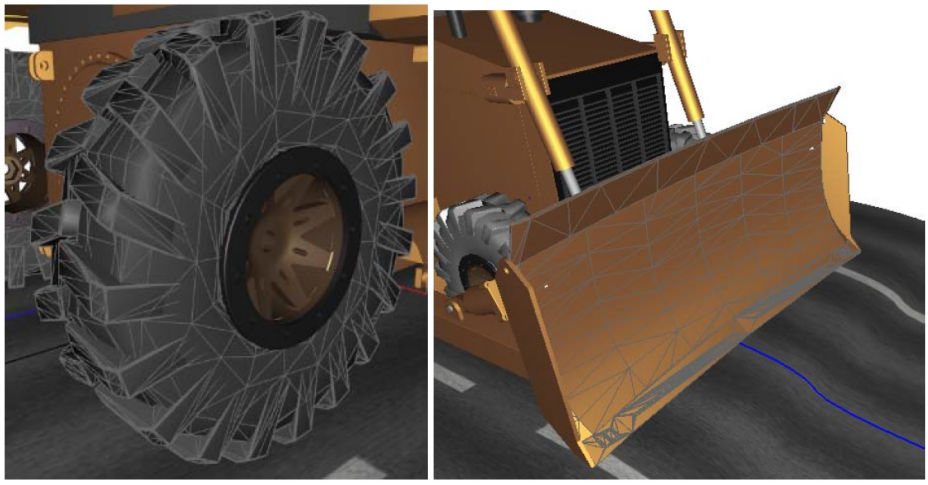

Figure 3.11. Bulldozer tire and blade polygonal contact surfaces.

are found. This recursive division continues until there is only one polygon in a box.

- For each master contact surface the contact points are divided into 2 blocks. The bounding sphere for each block of points is found. Then, each of those blocks of points is divided into 2 blocks and again the bounding spheres for those blocks are found. This recursive division continues until there is only one point (with a bounding sphere of radius 0).

www.manaraa.com

During the solution the following steps are performed. For each master contact sphere, the radius of the contact sphere is added to the size of the bounding box, then we check if the center point of the sphere is inside a bounding box. If the center of the contact sphere is not inside any bounding box, then all the points inside that sphere are not in contact with the surface. If it is found that the center of the contact sphere is inside a bounding box then the two sub-bounding boxes are checked to determine whether the point is inside either one. If it's inside then the sub-contact spheres are checked. If a contact point is found to be inside the lowest level bounding box, then a more computationally intensive contact algorithm between a point and a polygon is used to determine the depth of contact and the local position of the contact point on the polygon.

3.3 Inter Particle Contact Search

One of the major component of the DEM model is search and detection of inter-particle contacts. In [54] [55] [56] a space decomposition algorithm was developed to speed up the search for particle contact. The steps of the algorithm are as follows:

1- The space where the particles can move is decomposed into a Cartesian Eulerian volume grid of equally sized boxes (Figure 3.12).

2- All the particles are looped over in the beginning. For each particle, the grid boxes that intersect the particle are found. The position of the center of the particle and the bounding box of the particle can be used to determine the minimum and maximum vertical and horizontal grid numbers of a particle. In supplement to this, each grid box has a list of particles that it intersects. Thus, in the same loop for each grid box that intersects the particle we add the particle to the grid box.

3- For each particle a list of neighboring particles that can come into contact with a particle is generated. This list consists of the particles that intersect the boxes that the particle intersects.

www.manaraa.com

4- For each particle, the distance between the center of the particle and the center of a neighboring particle is calculated. If that distance is larger than the sum of bounding sphere radii of the two particles, then the particles are not in contact. Otherwise the particles may be in contact and a detailed contact point detection is carried out to find the contact point (if any).

5- 5- The algorithm maintains a record of the boxes that contain particles. Only those boxes are initialized to zero particles each time step. This must be done, since the number of Cartesian boxes is typically much larger than the number of particles. So the algorithm must not keep initializing boxes that have zero particles each time step. The main algorithm loop is over the number of particles N. Thus, particle search algorithm is O(N) instead of O(N^2) for an algorithm where each particle is checked against all other particles. The additional bounding sphere search quickly eliminates most of the neighboring particles thus the particles that the most computationally expensive contact point detection is carried over are the neighboring particles that have a very high likelihood of being in contact with the particle.

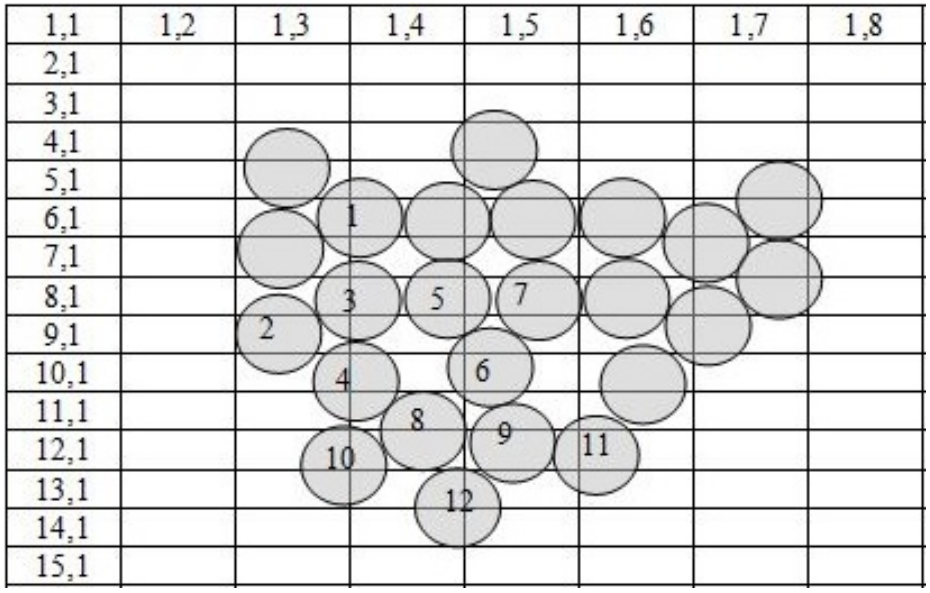

Figure 3.12. Cartesian grid domain decomposition.

www.manaraa.com

4. BULLDOZER MODEL

The DIS [67] explicit-time integration finite element code was used to create the coupled multibody dynamics model of the bulldozer and DEM soil model and to generate the simulation results. A description of the bulldozer and soil models is presented in this chapter.

4.1 Bulldozer Multibody Dynamics Model

Figure 4.1 shows the bulldozer multibody dynamics model. It consists of 15 rigid bodies: main chassis; 4 wheels; blade; blade C-frame; 4 hydraulic cylinders; and 4 hydraulic pistons (Figure 4.2). Table 4.1 shows the masses and moments of inertia of the bulldozer rigid bodies. The bodies are connected using revolute joints and cylindrical joints. Four linear actuators with PD controllers are used to control the position and angles of the blade. A rear wheel drive bulldozer model has two rotary actuators with PD controllers at the rear wheels used to propel the vehicle. A 4-wheel drive bulldozer model has four rotary actuators with PD controllers at all the wheels.

The total mass of the vehicle is 9,260 kg for the rear wheel drive vehicle and 9,480 kg for the four wheel drive vehicle. For the rear wheel drive vehicle the mass of each front wheel is 80 kg and its diameter is 1.16 m , the mass of each rear wheel is 300 kg and its diameter is 1.44 m. For the four wheel drive vehicle all the wheels have the same mass and diameter of 300 kg and 1.44 m respectively. Each tire polygonal surface consists of 6662 triangles (Figure 3.11). The tire's surfaces are set as slave contact surfaces for the DEM particles.

www.manaraa.com

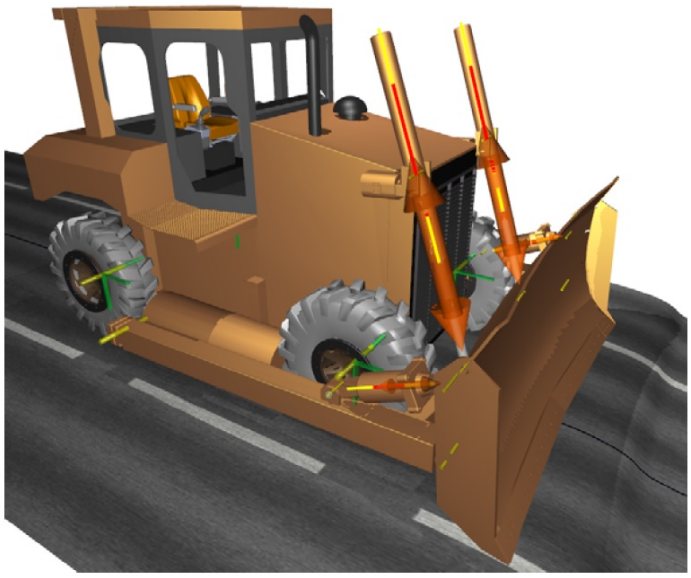

Figure 4.1. 4-wheel drive bulldozer model.

4.2 Soil Model

The DEM soil material properties are listed in Table 4.2. The DEM model has 582,232 point-type particles with a particle diameter of 3 cm. The soil particles are inside a bounding box that is 8.5 m long, 4.5 m wide and 1.5 m high (Figure 4.3). The box has a flat rectangular lid shown in blue in Figure 4.3 with a prismatic joint and a linear actuator. The lid is used to level and compress the particles. A Cartesian search grid with a resolution of 283 (length), 150 (width) and 50 (height) is used (Figure 4.4). The side length of a grid cell was chosen to be equal to the diameter of the particle.

4.3 Simulation Conditions

Table 4.3 shows a summary of the main parameters of the bulldozer soft soil run. A run starts by letting the rectangular array of particles fall in the bounding box (representing the ground) for 0.5 sec and at the same time the rectangular lid is used to apply a uniform pressure of 33,333 Pa in order to plastically compress the soil to

www.manaraa.com

Figure 4.2. DIS hierarchy of the bulldozer model.

the desired bulk density and to increase the soil's cohesive strength. At time 1 sec the lid is removed. Starting at time 0 the drive wheels desired angular velocity is ramped up from 0 to 2.286 rad/sec in 3 sec. The bulldozer wheels start running on the soil

www.manaraa.com

Table 4.1. 4-wheel drive bulldozer model components mass and moment of inertia.

No	Part Name	Mass(kg)	I_{xx}(kg-m$\hat{2}$)	I_{yy}(kg-m$\hat{2}$)	I_{zz}(kg-m$\hat{2}$)
1	Chassis	7000	15750	10937	6317.5
2	Bulldozer Blade	500	7.8125	101.25	28.2
3	C-Fram	400	169	169	81
4	Lower Left Hyd. Cylinder	80	7.2	7.2	1.352
5	Lower Left Hyd. Piston	30	1.2	1.2	0.1
6	Lower Right Hyd. Cylinder	80	7.2	7.2	1.352
7	Lower Right Hyd. Piston	30	1.2	1.2	0.1
8	Upper Left Hyd. Cylinder	100	9	9	0.1407
9	Upper Left Hyd. Piston	80	4.05	4.05	0.1
10	Upper Right Hyd. Cylinder	100	9	9	0.1407
11	Upper Right Hyd. Piston	80	4.05	4.05	0.1
12	Left Front Wheel	200	12	12	12
13	Right Front Wheel	200	12	12	12
14	Left Rear Wheel	300	25	25	25
15	Right Rear Wheel	300	25	25	25
	Total Mass	9480			

patch at around time 3.0 sec. The blade starts penetrating the soil around time 3.24 sec.

www.manaraa.com

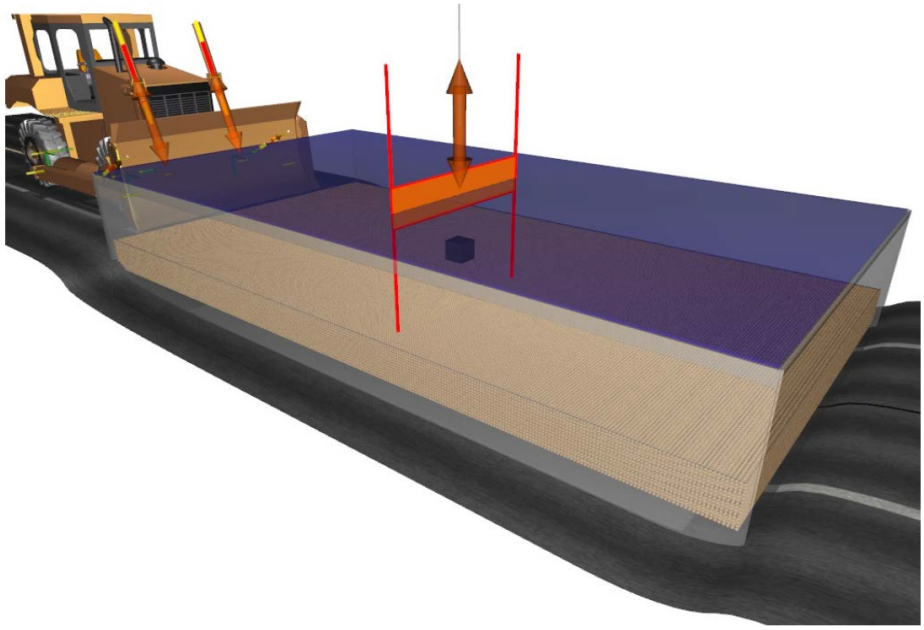

Figure 4.3. DEM particles inside a box with a rectangular lid (shown in blue).

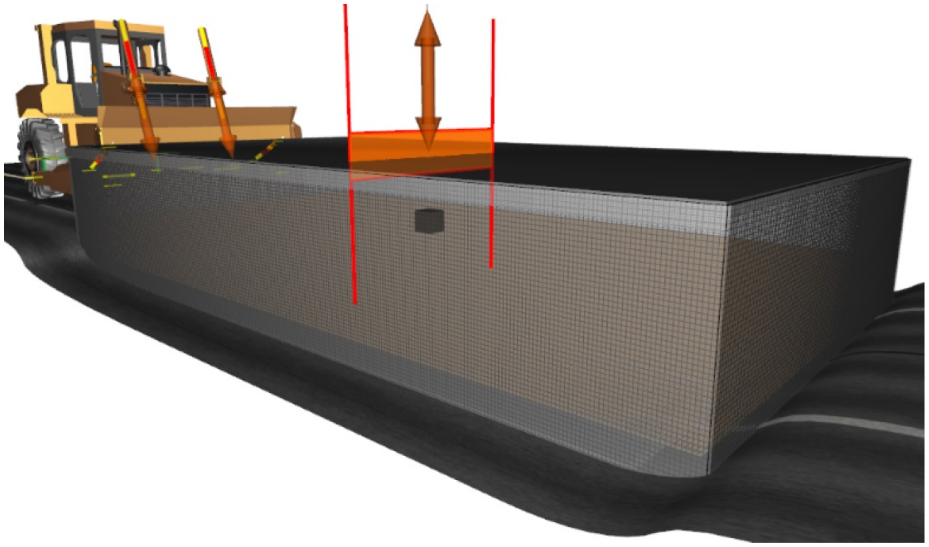

Figure 4.4. Search grid around the particle box.

www.manaraa.com

Table 4.2. Baseline DEM soil material properties.

Particle Diameter	3.0 cm
Particle mass	0.0254475 kg
Inter-particle friction coefficient (μ)	0.175
Particle to tire friction coefficient	0.6
Friction velocity stiffness	1500 N.s
Viscosity coefficient (c_t)	0
Normal damping coefficient (c_n)	500 N.s
Separation damping factor (s_n)	0.05
Normal stiffness (slope of repulsion force) (Figure 3.2)	1.3 x 10^6 N/m Figure 4.5
Adhesion force versus penetration (Figure 3.2)	Figure 4.6
Maximum adhesion force versus plastic deformation (Figure 3.7)	Figure 4.7
Plastic deformation versus normal force (Figure 3.5 and 3.6)	Figure 4.8
Soil relaxation parameter	0.02 m/s

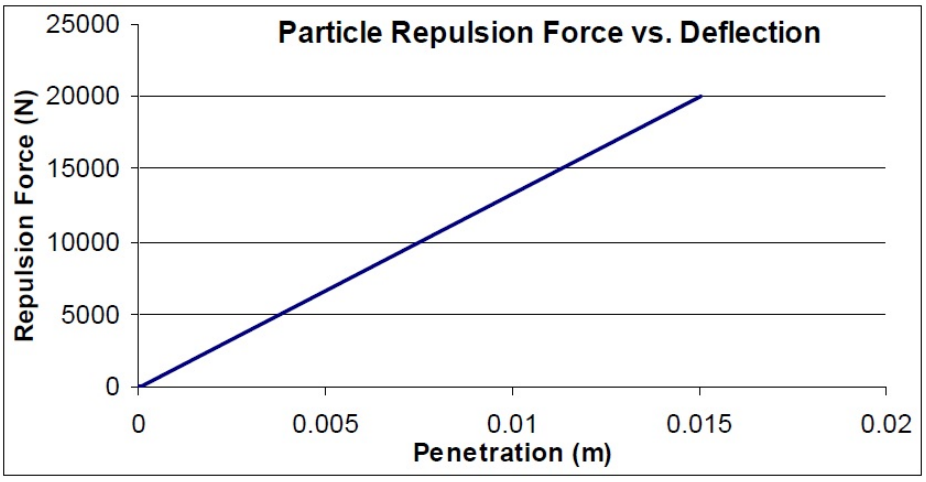

Figure 4.5. Repulsion force versus penetration (deformation).

www.manaraa.com

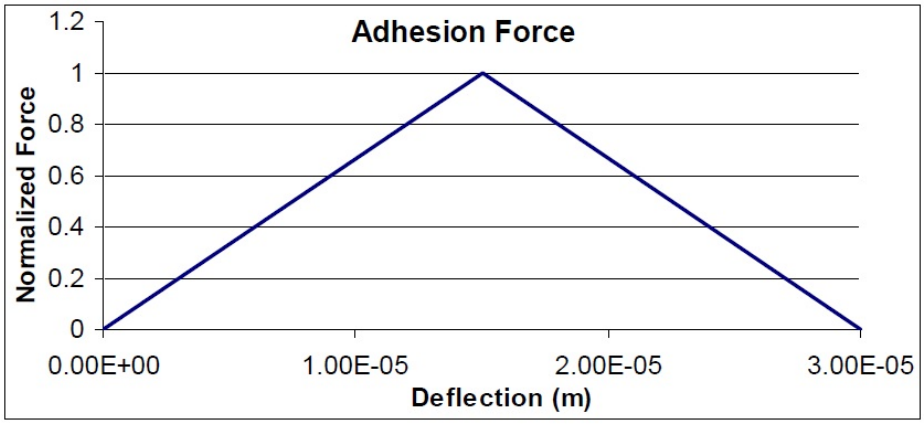

Figure 4.6. Normalized adhesion force versus particle deflection.

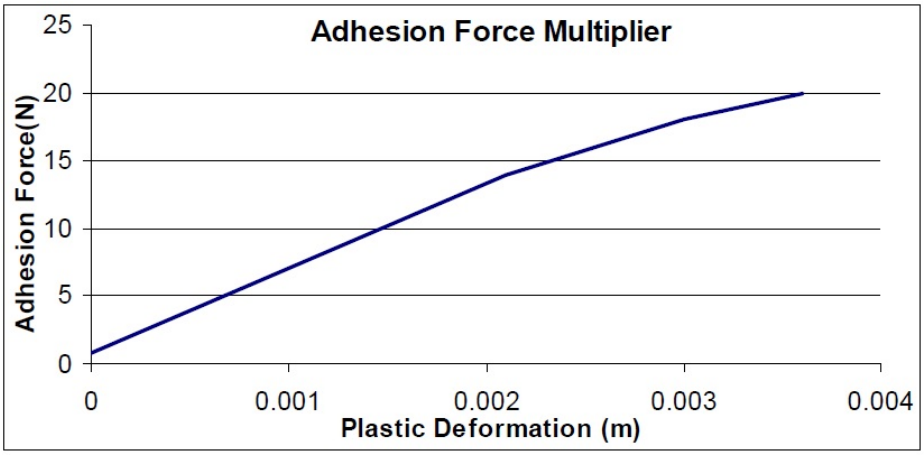

Figure 4.7. Adhesion force versus plastic deformation.

www.manaraa.com

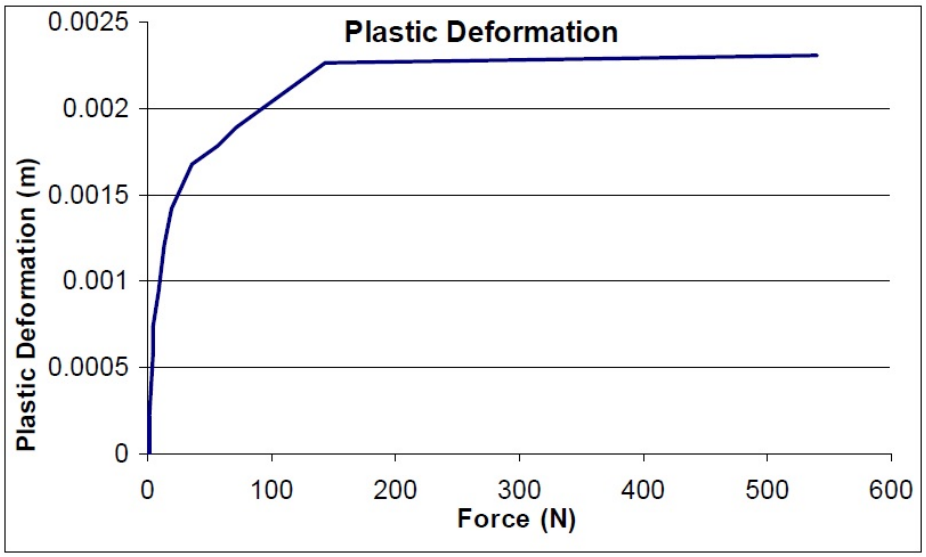

Figure 4.8. Plastic deformation versus repulsion force.

Table 4.3. Summary of a run conditions and parameters.

Number of rigid bodies in the bulldozer	15
Numbers of the DEM particles	582,232
Gravity	9.8 m/s^2 downwards
Eulerian particle box resolution	283 x 150 x 50
Eulerian particle box size	8.5 m x 4.5 m x 1.5 m
Simulation time step	1.0 x 10^{-5} sec
Explicit iterations	1
Computer time (hours/sec of simulation time) (run was performed on 16 CPU cores (2 x 2.6 GHz Intel Xeon E5-2670 8 core)	4.6 hours/sec
Total simulation time	14 sec

www.manaraa.com

5. RESULTS AND DISCUSSION

The following simulation are performed (Table 5.1):

1- Rear wheel-drive vehicle.

2- 4-wheel drive vehicle with two blade soil penetration depths.

3- 4-wheel drive vehicle with three values of the soil relaxation parameter.

Table 5.1. Bulldozer simulations performed.

Run No.	Drive Type	Soil Penetration Depth		Relaxation Parameters (m/s)		
		4 cm	5 cm	0.0	0.02	0.1
1	Rear-Wheel Drive	✓			✓	
2	4-Wheel Drive	✓			✓	
3	4-Wheel Drive		✓	✓		
4	4-Wheel Drive		✓		✓	
5	4-Wheel Drive		✓			✓

5.1 Rear Wheel-Drive Vehicle

Figures 5.1 and 5.2 show snapshots from the simulation. Figure 5.3 shows a snapshot of the soil at time 13 sec. The figure shows the tracks of the bulldozer's wheels and the material pile in front of the blade. Figure 5.4 shows the time-history of the bulldozer's speed. Figures 5.5 and 5.6 show the time-history of the angular velocities of the rear and front wheels respectively. Figure 5.7 shows the time-history of the applied rear wheel torque. Initially, when the bulldozer is on hard pavement, the bulldozer accelerates to about 1.5 m/s by controlling the rear wheel's angular

www.manaraa.com

velocity until it reaches a speed of 2 rad/s. Then, the front wheels start going over the soil patch at about time 3.2 sec. The rear wheel starts to slip due to the resistance of the soil and the vehicle speed decreases. The blade starts to dig into the soil at time 4.5 sec and the vehicle speed decreases further. As the material pile in front of the bulldozer gets larger and the bulldozer blade penetration in the soil gets deeper, the rear wheels slip increases and the bulldozer slows down until it reaches a steady speed of about 0.12 m/sec. At time 11.8 sec the rear wheels start going over the soil patch. The bulldozer initially speeds up because the pavement is slightly higher than the soil patch, then the speed reduces again due to the resistance of the soil to the wheels and blade of the bulldozer. This simulation shows that a rear wheel drive bulldozer has a limited digging capacity compared to the 4-wheel drive bulldozer shown in the next sections.

5.2 4-Wheel-Drive Vehicle – Effect of Soil Penetration Depth

Two soil penetration depths were simulated using the 4-wheel drive bulldozer in order to assess the effect of the soil penetration depth on the bulldozer and soil responses. The low soil penetration depth of about 4 cm is achieved by raising the blade 5 cm from the nominal position. The high soil penetration depth of about 5 cm is achieved by raising the blade 4 cm from the nominal position. So the difference between the high and low depth is only 1 cm.

Figures 5.8 to 5.11 show snapshots from the simulation for the 4 cm (low) penetration depth. Figure 5.11 shows a snapshot of the soil with the bulldozer hidden at time 9.5 sec. The Figure 5.11 shows the tracks of the bulldozer's wheels and the material pile in front of the blade. Similarly Figure 5.12 to 5.14 show snapshots from the simulation for the 5 cm (high) penetration depth. Figure 5.14 shows a snapshot of the soil with the bulldozer hidden at time 12.5 sec.

Figure 5.15 shows the time-history of the bulldozer's speed for the 4 cm and 5 cm soil penetration cases. Also, the no soil vehicle speed is also shown in the

www.manaraa.com

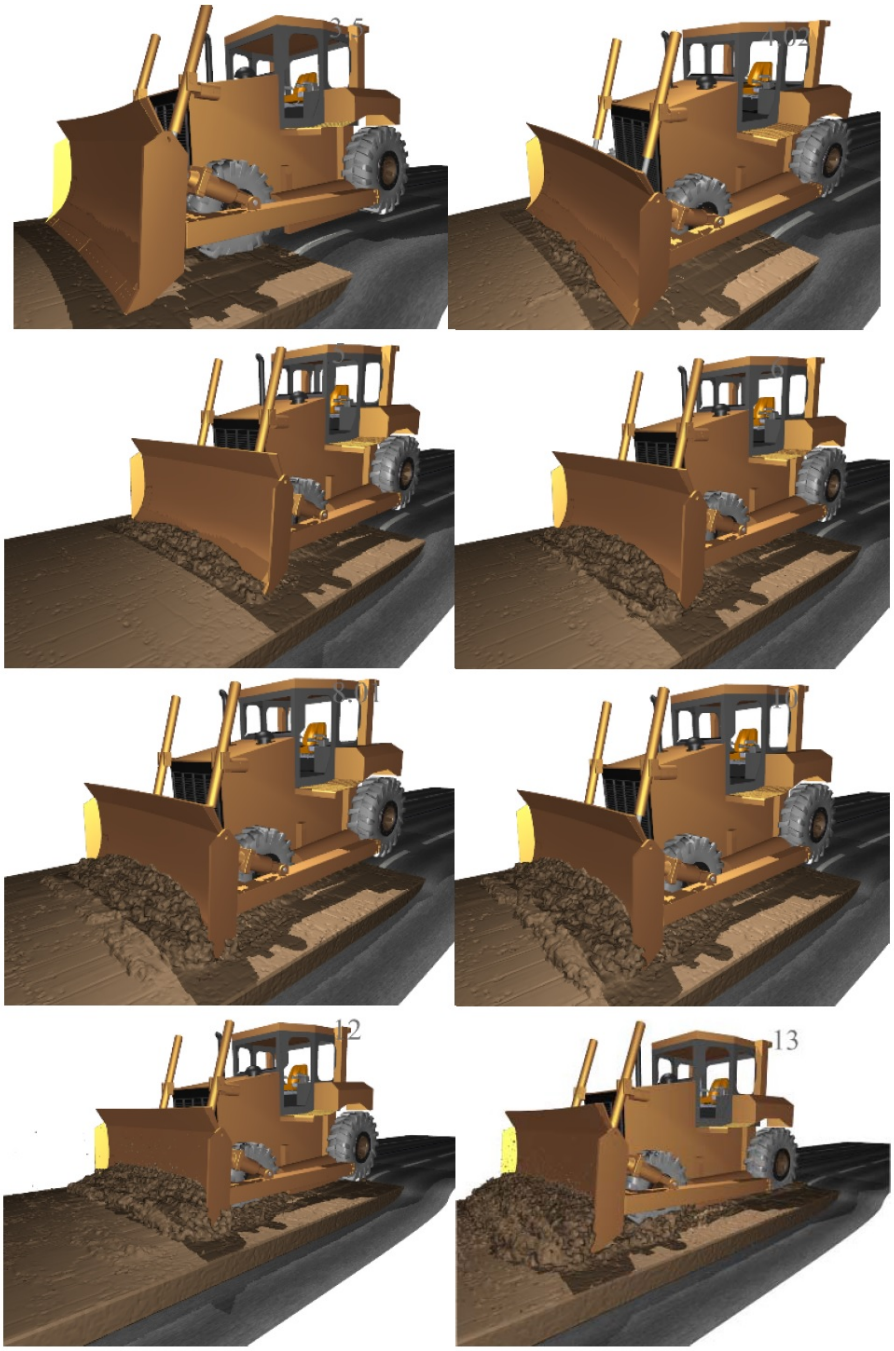

Figure 5.1. Snapshots of the rear wheel-drive bulldozer driving over a soft soil patch while digging a layer of soil. The soil is displayed as a density isosurface. Average soil penetration depth is about 4 cm and soil relaxation is 0.02 m/s.

www.manaraa.com

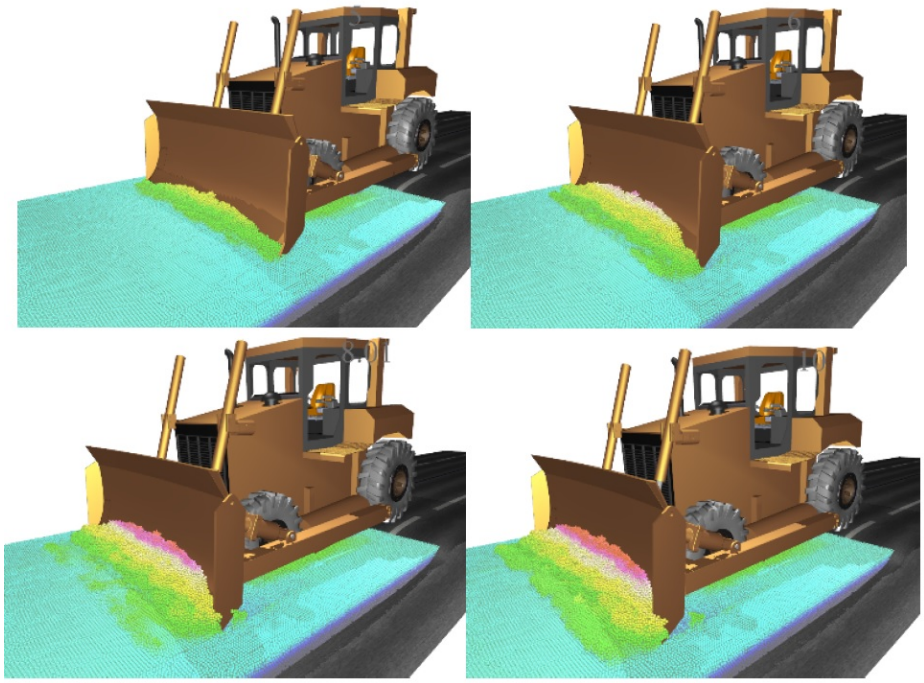

Figure 5.2. Snapshots of the rear wheel-drive bulldozer driving over a soft soil patch while digging a layer of soil. The soil is displayed using particles colored using height.

figure for comparison. Similarly, Figures 5.16 and 5.17 show the time-history of the angular velocities of the rear and front wheels, respectively. Figure 5.18 and 5.19 show the time-history of the applied wheel torque of rear and front wheels, respectively. Initially, when the bulldozer is on hard pavement, the bulldozer accelerates to about 1.5 m/s by controlling rear and front wheel's actuators and angular velocities of rear and front wheels reaches to an angular speed of 2.25 rad/s. Then, the front wheels start going over the soil patch at about time 3.0 sec and the blade start going through the soil at time 3.24 sec. The velocity of bulldozer starts reducing from 3.0 sec to 5 sec because of front wheel soil resistance and pile formation of soil in front of blade and reduces to nearly 1 m/s. It rises up again to nearly 1.28 m/s at 5.6 sec, because the rear wheel moves down from the pavement to the soil and because when all wheels are on the soil and they give better traction. Then, as the bulldozer blade

www.manaraa.com

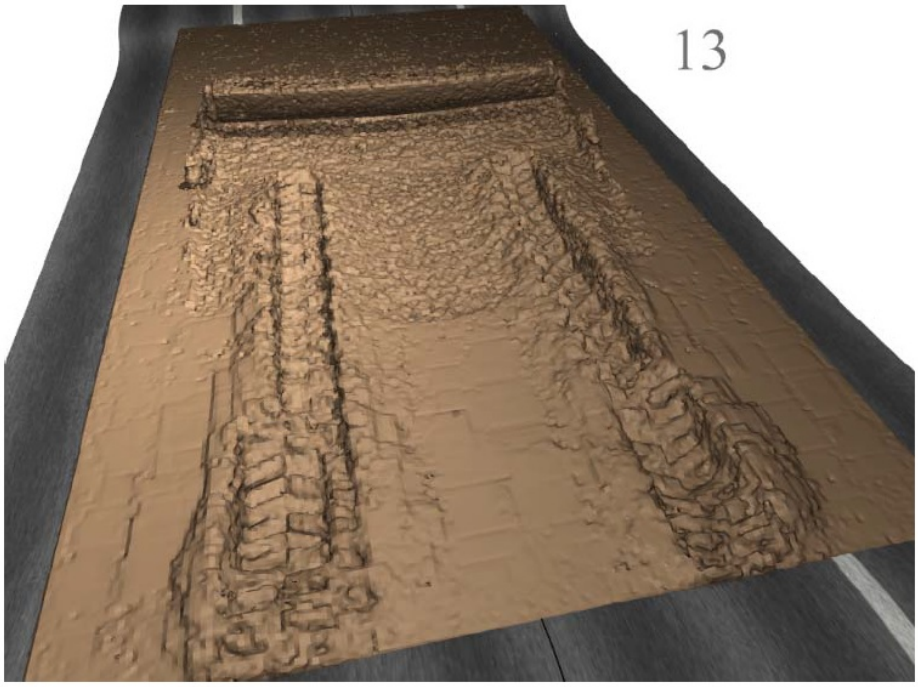

Figure 5.3. Snapshot of the soil at time 13 sec with the bulldozer hidden.

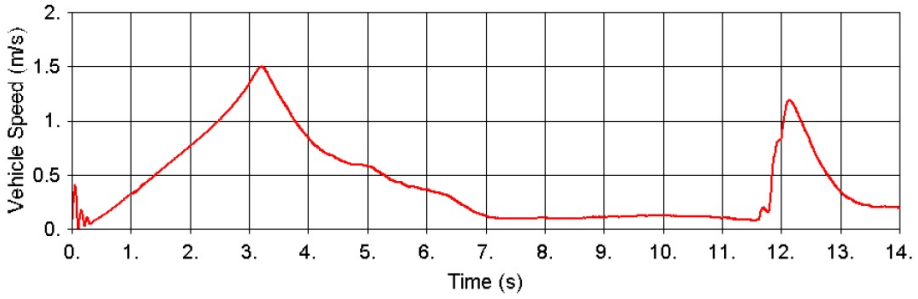

Figure 5.4. Time-history of the rear wheel-drive bulldozer speed.

digs through the soil which results into pile formation, the velocity of bulldozer starts decreasing and the rear wheel starts to slip due to the resistance of the soil. For the low penetration depth run the bulldozer slows down to a steady speed of about 0.6 m/s till the end of the soil patch at time about 10 sec, while all the bulldozer wheels are slipping over the soil. For the high penetration depth run the bulldozer speed reaches almost 0.05 m/s and then oscillates a couple of times between 0.05 and 0.4

www.manaraa.com

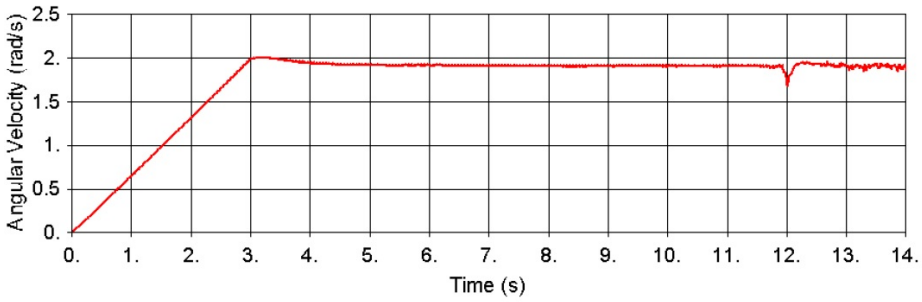

Figure 5.5. Time-history of the angular velocity of the rear wheels for the rear wheel-drive bulldozer.

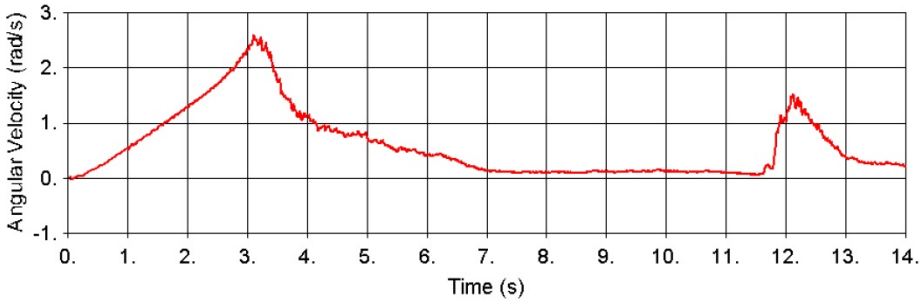

Figure 5.6. Time-history of the angular velocity of the front wheels for the rear wheel-drive bulldozer.

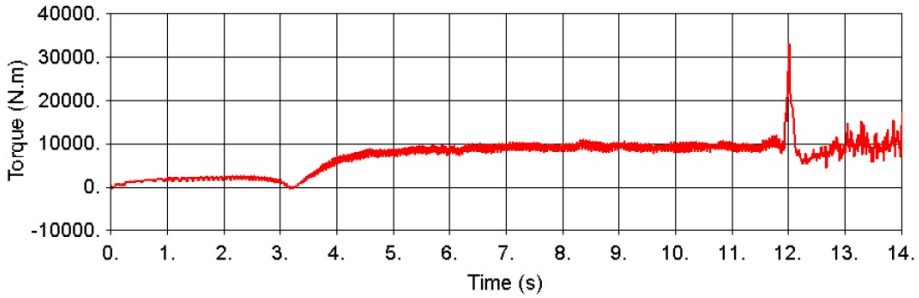

Figure 5.7. Time-history of a rear wheel applied torque for the rear wheel-drive bulldozer.

m/s. Due to the fact that the bulldozer is moving slower, the bulldozer reaches the end of the soil patch at time 13.5 sec. Figure 5.15 shows that velocity of vehicle is on average much higher in case of lower penetration depth than higher penetration depth. In addition, higher torque is required in case of higher penetration depth.

www.manaraa.com

Figures 5.20 and 5.21 show the time-history of the upper and lower actuator forces respectively. The displacement of the upper and lower hydraulic actuators is plotted against time in Figures 5.22 and 5.23. The difference in penetration depth can be observed from Figure 5.22.

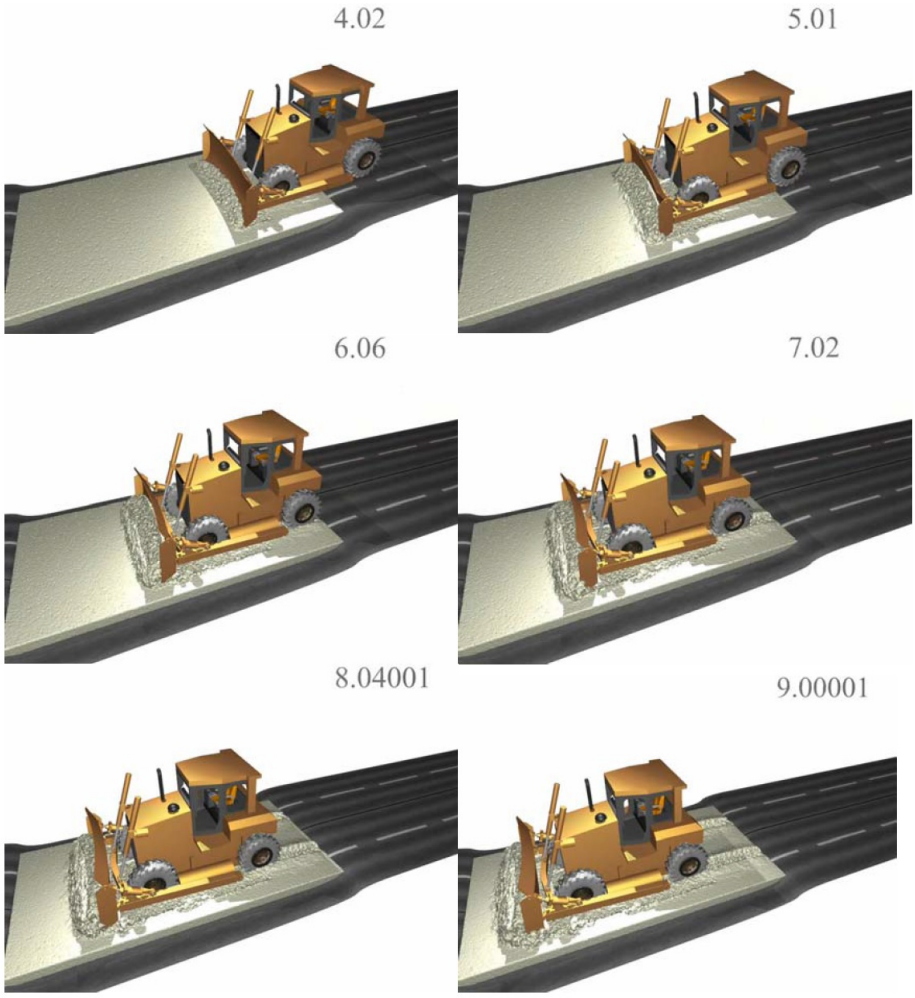

Figure 5.8. Side view snapshots from time 4 to 9 sec of the bulldozer digging a soil layer – 4 cm avg. blade penetration, 0.02 m/s adhesion relaxation speed.

www.manaraa.com

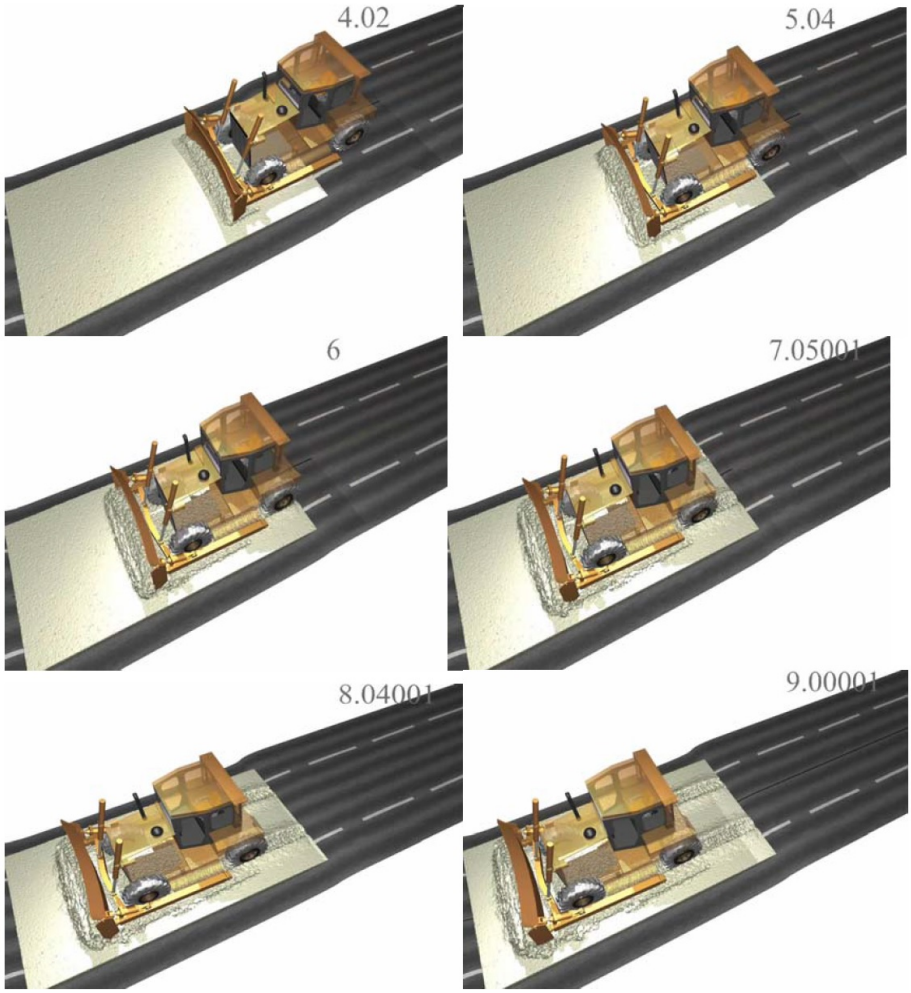

Figure 5.9. Top view snapshots from time 4 to 9 sec of the bulldozer digging a soil layer – 4 cm avg. blade penetration, 0.02 m/s adhesion relaxation speed.

5.3 4-Wheel-Drive Vehicle – Effect of Soil Relaxation

In this experiment, soil relaxation parameter is varied using the values: 0, 0.02 and 0.1 m/s. The high soil penetration depth of 5 cm is used (by raising the blade 4 cm from the nominal position) for all the simulations. Figures 5.12 to 5.14 show snapshots of the 0.02 m/s relaxation speed, Figures 5.24 to 5.26 show snapshots of the 0 m/s relaxation speed. Figures 5.27 to 5.29 show snapshots of the 0.1 m/s relaxation speed. Figure 5.30 shows the comparison of bulldozer's speed at different relaxation

www.manaraa.com

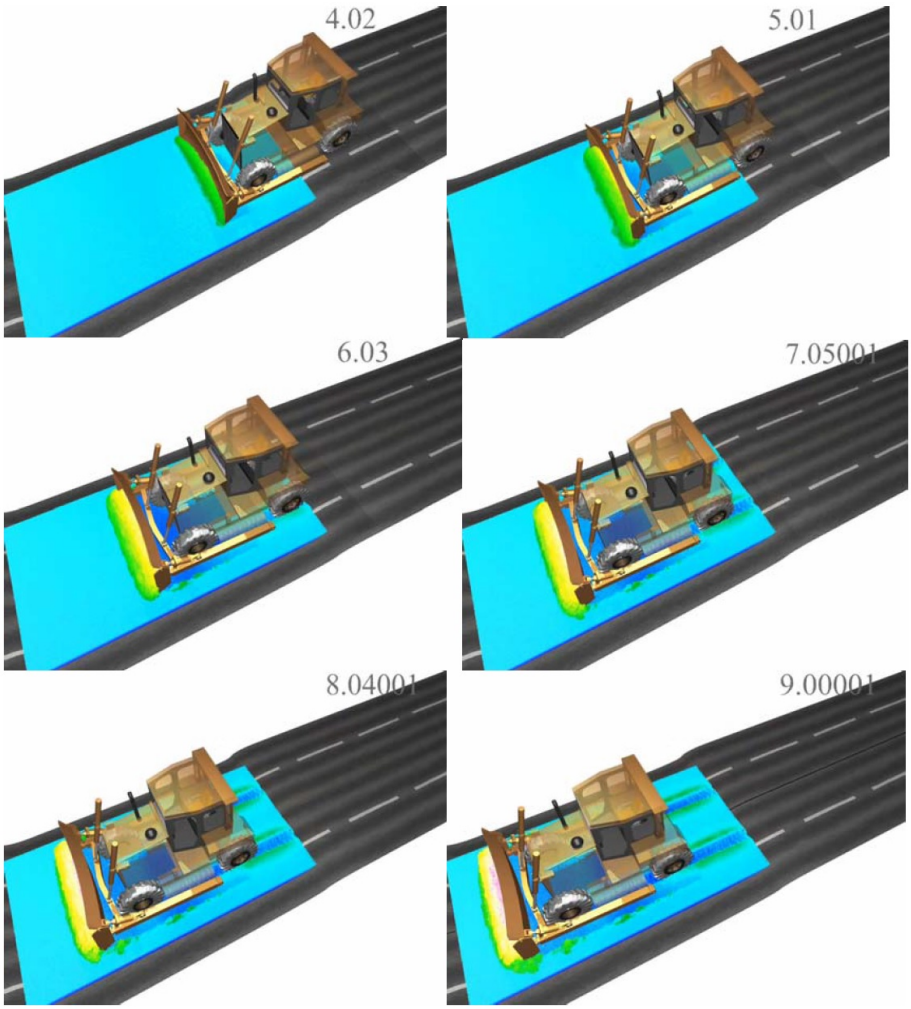

Figure 5.10. Colored elevation view from time 4 to 9 sec of the bulldozer digging a soil layer – 4 cm avg. blade penetration, 0.02 m/s adhesion relaxation speed.

parameters. Figures 5.31 and 5.32 show the time-history of the angular velocities of the rear and front wheels respectively. Figures 5.33 and 5.34 show the time-history of the applied wheel torque of rear and front wheels respectively. Initially, bulldozer accelerates to 1.5 m/s when it's on the hard pavement. Angular velocity of all wheels at time 3 sec is equal to 2.25 m/s. Then front wheels start going over the soil patch at about 3.0 sec. The velocity of bulldozer starts reducing and it reaches about 0.9 m/s at time 5 sec, due to pile formation in front of the blade and front wheel

www.manaraa.com

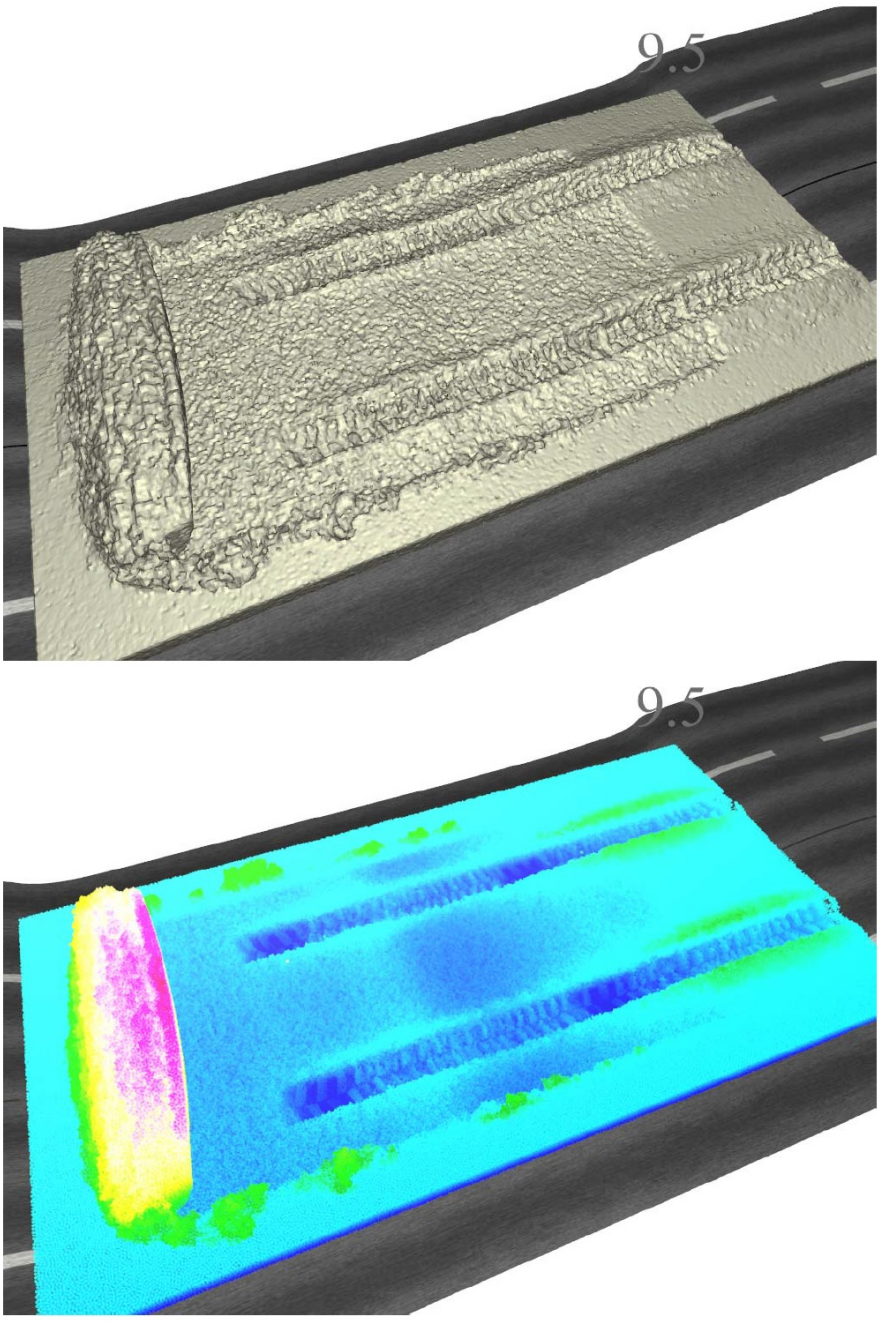

Figure 5.11. Top view snapshots at time 9.5 sec of the bulldozer digging a soil layer – 4 cm avg. blade penetration, 0.0 m/s adhesion relaxation speed.

soil resistance. The effect of the relaxation parameter can be easily observed from the variation in the Bulldozer's velocity. The higher the relaxation parameter, the

www.manaraa.com

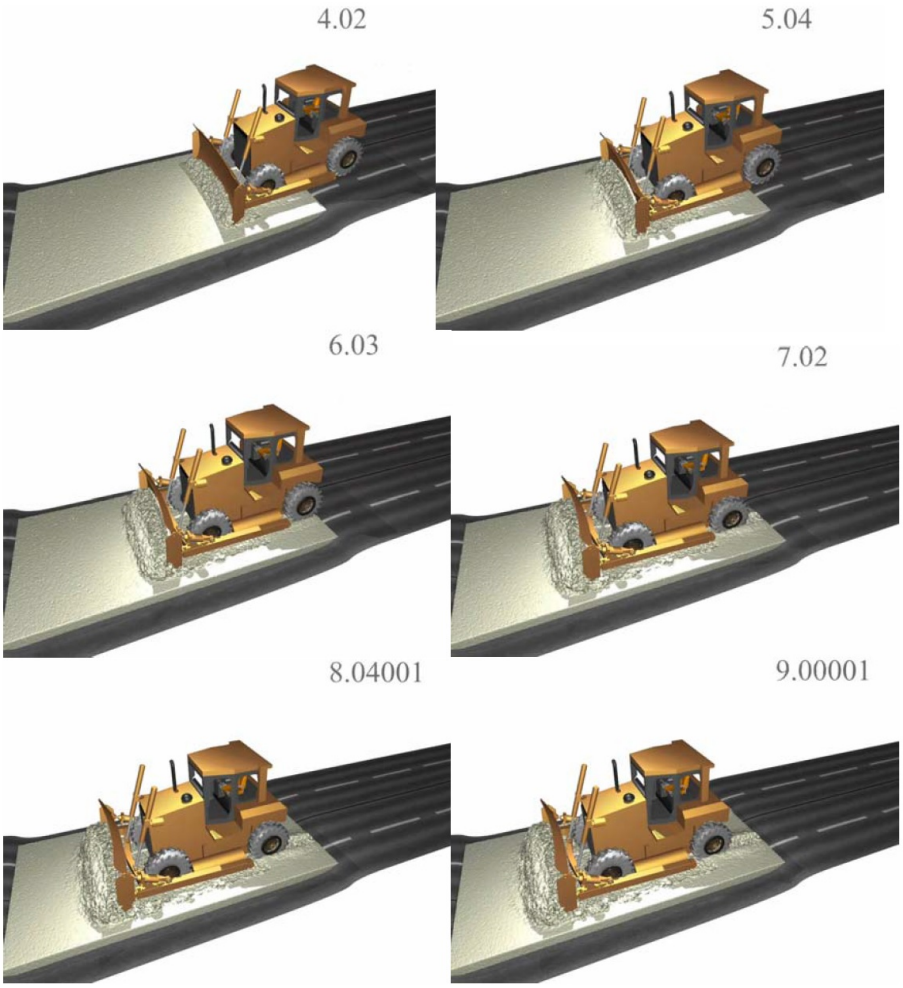

Figure 5.12. Side view snapshots from time 4 to 9 sec of the bulldozer digging a soil layer – 5 cm avg. blade penetration, 0.02 m/s adhesion relaxation speed.

higher is the bulldozer's velocity while it is crossing over the soil patch. The pile formed in front of the blade offers a resistance to bulldozer's motion. As the material pile in front of the blade gets larger, rear as well as front wheels start to slip and bulldozer loses traction. For the relaxation parameter equal to 0.0 and 0.02 m/s, bulldozer's speed reaches a minimum of about 0.05 at time 9 sec. It is observed that for the relaxation parameter equal to 0.1 m/s, bulldozer's speed is nearly 0.5 m/s at time 9 sec. The movement of the bulldozer through the soil patch is affected by the relaxation parameter. In case of higher relaxation parameter, the bulldozer reaches

www.manaraa.com

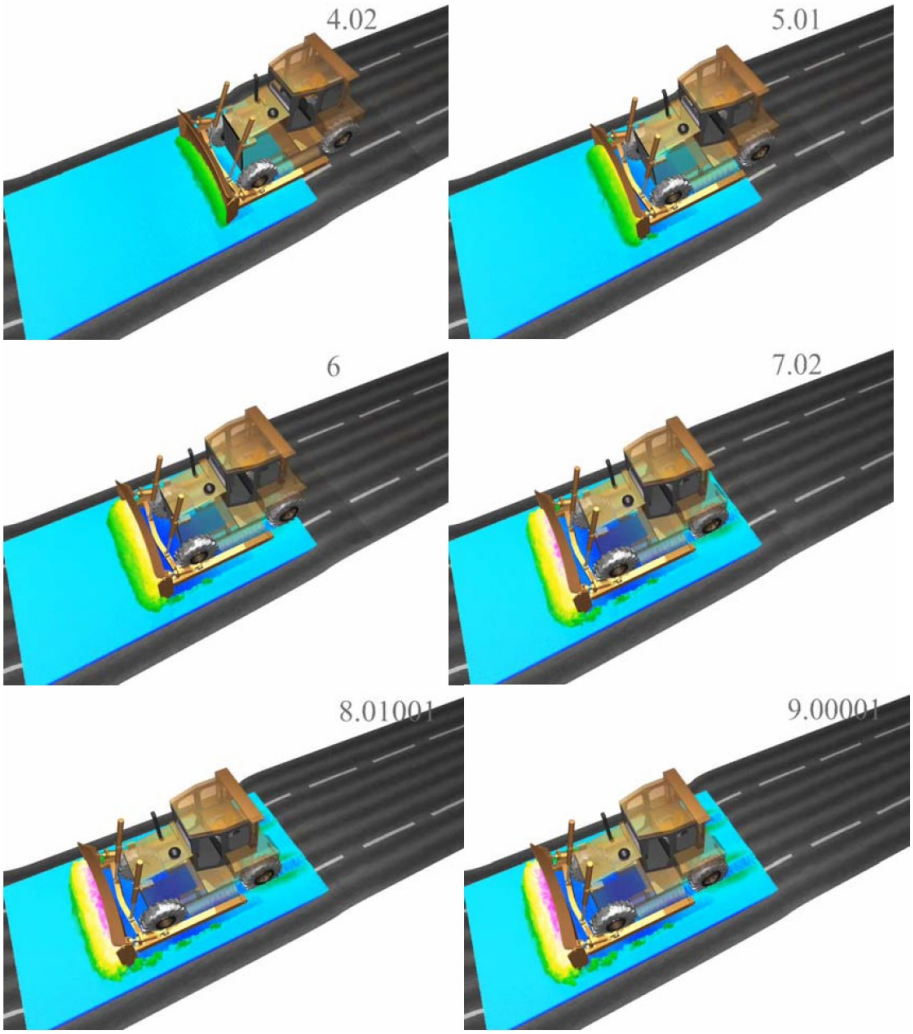

Figure 5.13. Colored elevation view from time 4 to 9 sec of the bulldozer digging a soil layer – 5 cm avg. blade penetration, 0.02 m/s adhesion relaxation speed.

the end of soil patch at time 11 sec. For the 0.02 m/s and 0 m/s relaxation parameter the bulldozer reaches the end of soil patch at time 13.5 sec and 15 sec respectively. Upper and lower hydraulic actuator forces are plotted against time in Figures 5.35 and 5.36 respectively. The displacement of the upper and lower hydraulic actuators is plotted against time in Figures 5.37 and 5.38.

www.manaraa.com

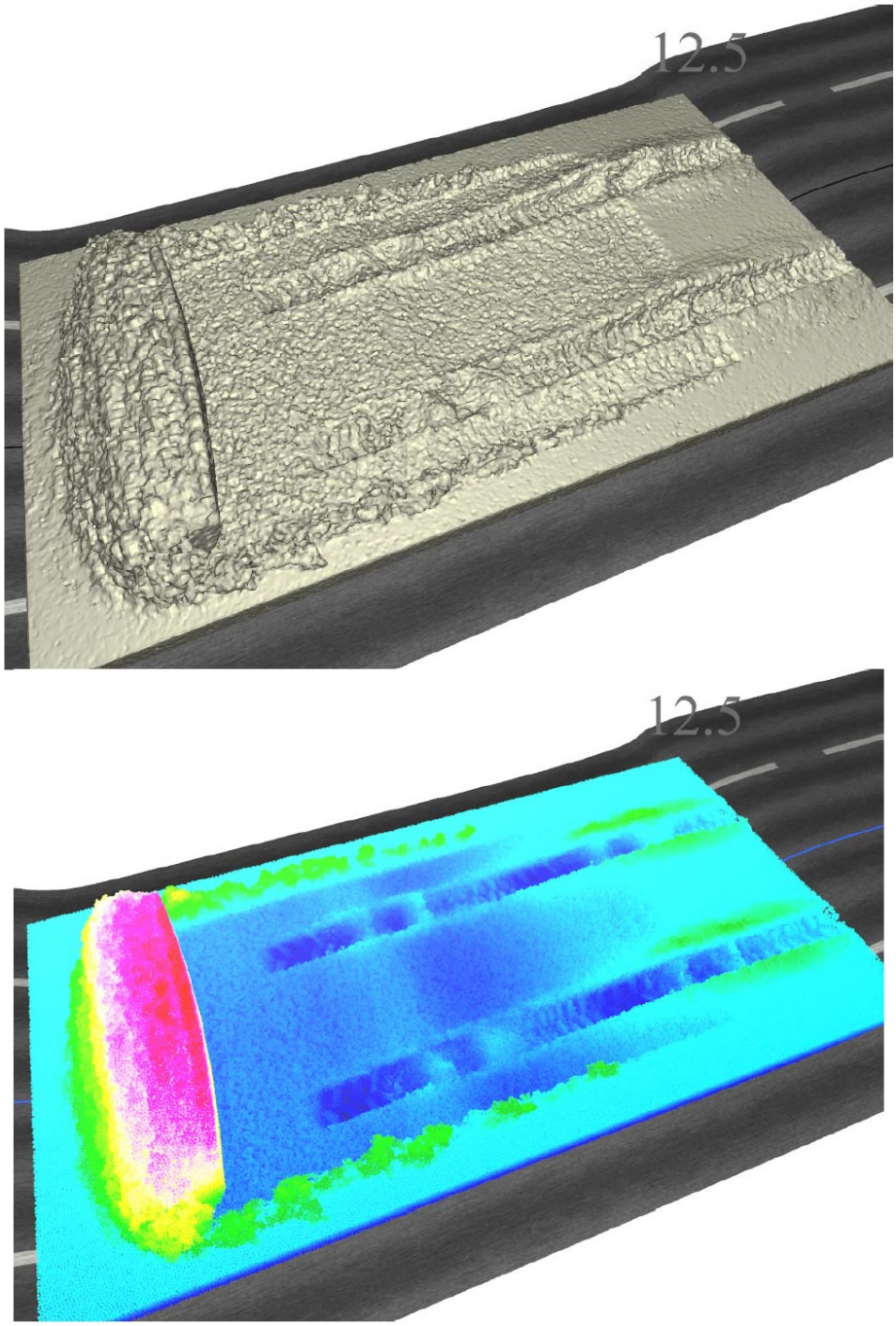

Figure 5.14. Top view snapshots at time 12.5 sec of the bulldozer digging a soil layer – 5 cm avg. blade penetration, 0.02 m/s adhesion relaxation speed.

www.manaraa.com

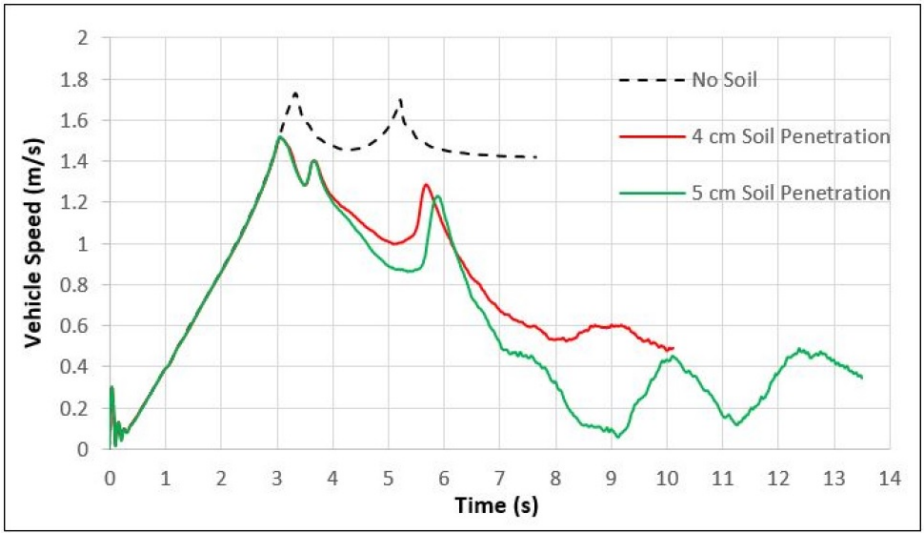

Figure 5.15. Time history of the 4-wheel drive bulldozer speed as function of blade soil penetration depth.

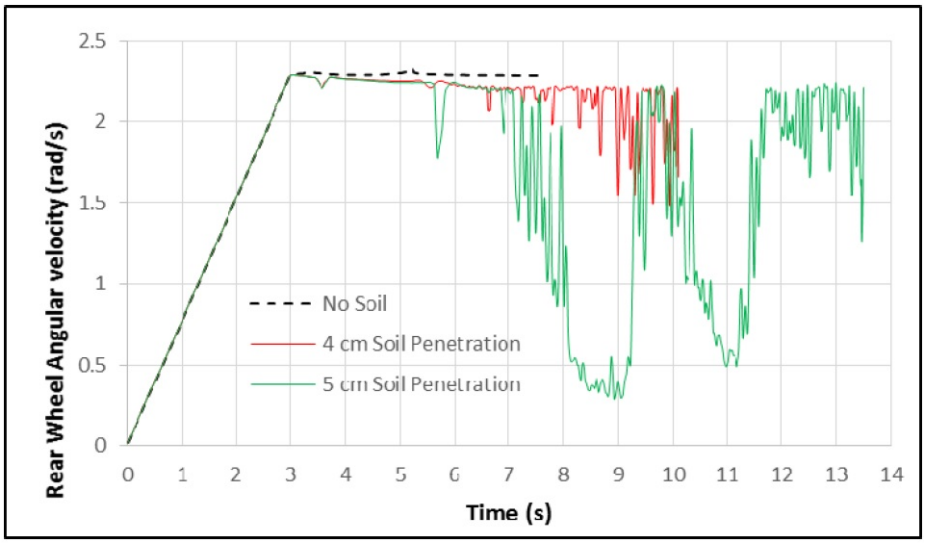

Figure 5.16. Time-history of the angular velocity of the rear wheels for the 4-wheel drive bulldozer as a function of penetration depth.

www.manaraa.com

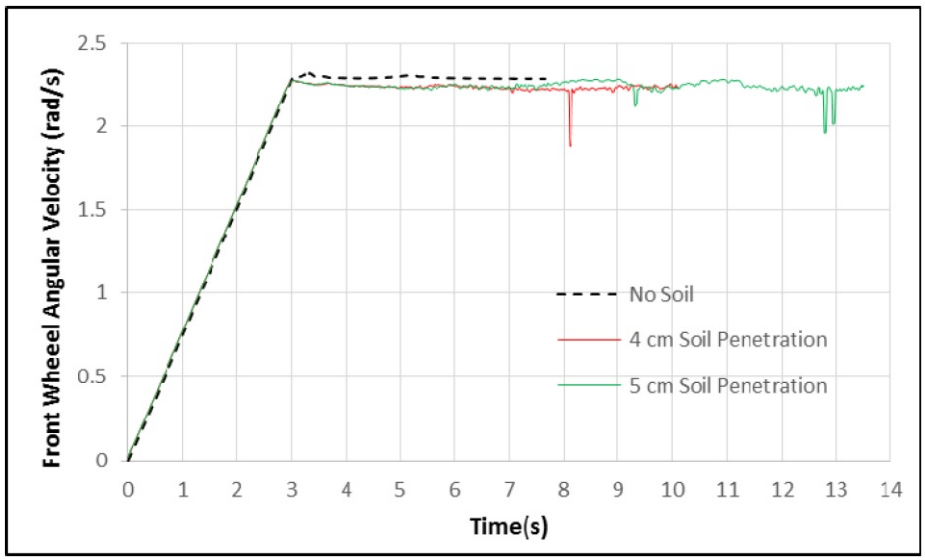

Figure 5.17. Time-history of the angular velocity of the front wheels for the 4-wheel drive bulldozer as a function of penetration depth.

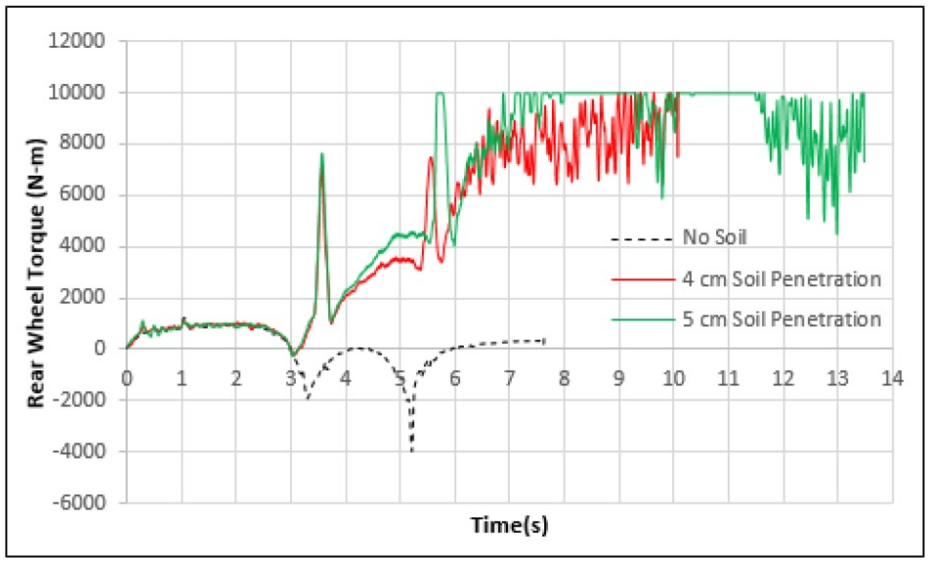

Figure 5.18. Time-history of a rear wheel applied torque for the 4-wheel drive bulldozer as a function of penetration depth.

www.manaraa.com

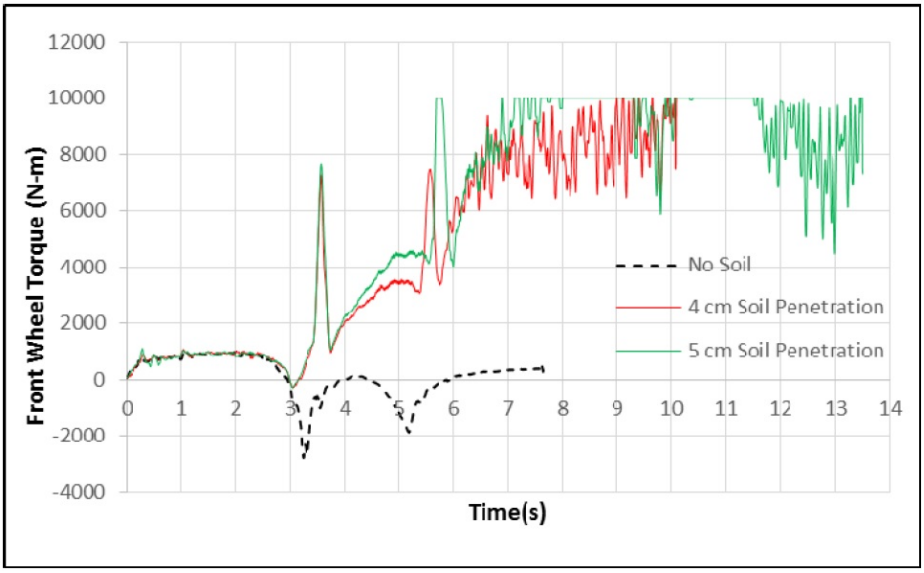

Figure 5.19. Time-history of the front wheels applied torque for the 4-wheel drive bulldozer as a function of penetration depth.

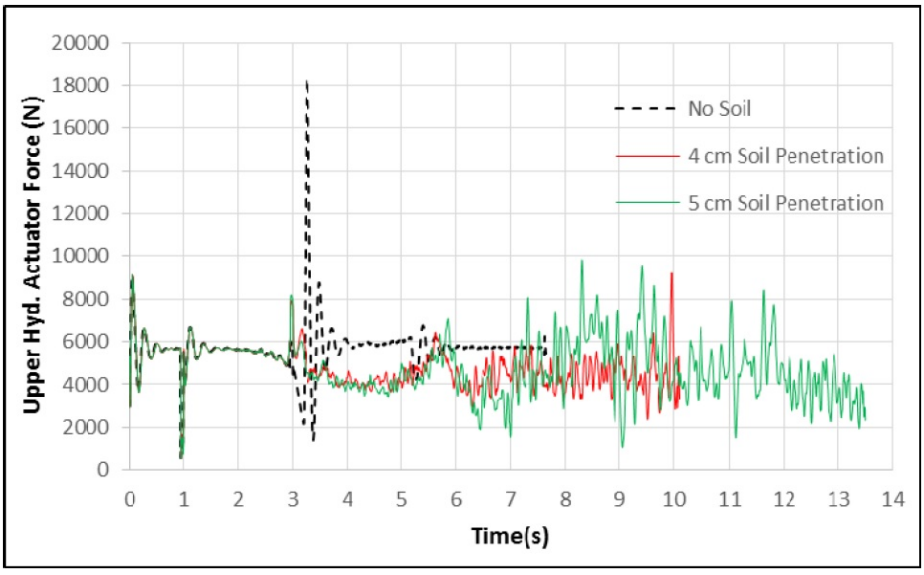

Figure 5.20. Time-history of the upper actuator force for the 4-wheel drive bulldozer as a function of penetration depth.

www.manaraa.com

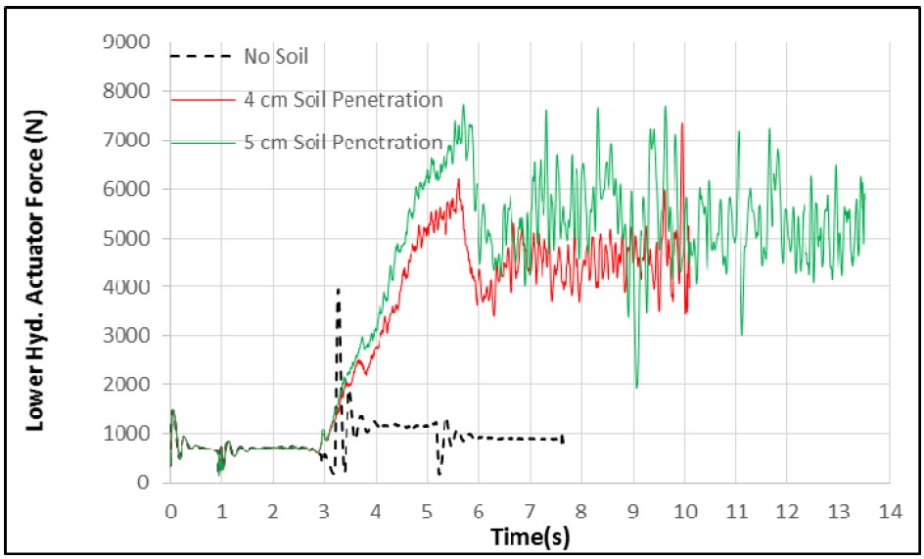

Figure 5.21. Time-history of the lower actuator force for the 4-wheel drive bulldozer as a function of penetration depth.

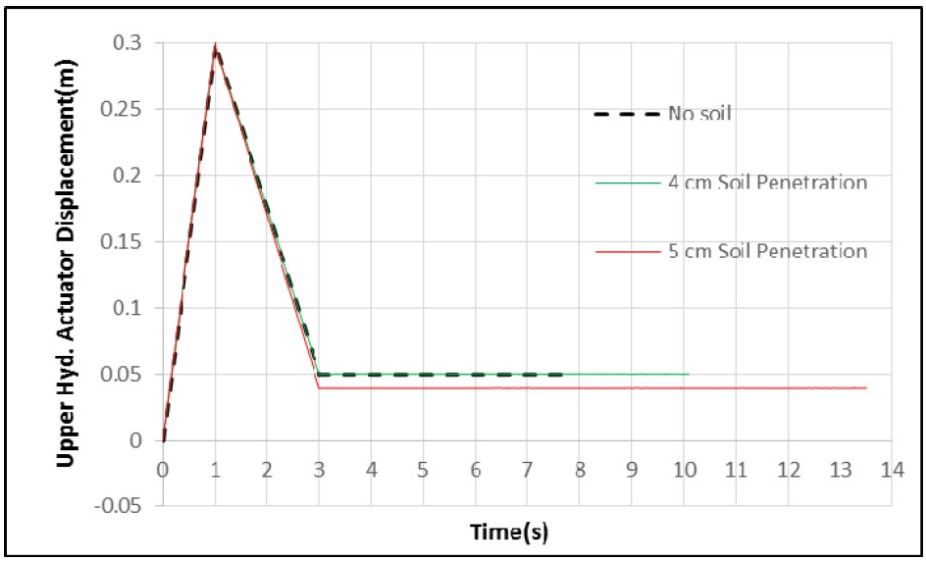

Figure 5.22. Time-history of the upper hydraulic actuator's displacement for the 4-wheel drive bulldozer as a function of penetration depth.

www.manaraa.com

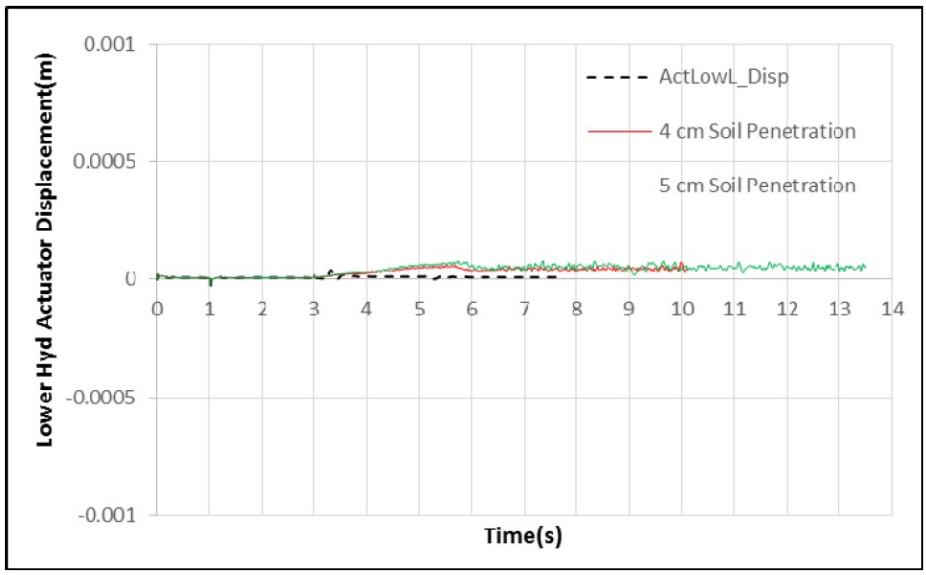

Figure 5.23. Time-history of the lower hydraulic actuator's displacement for the 4-wheel drive bulldozer as a function of penetration depth.

www.manaraa.com

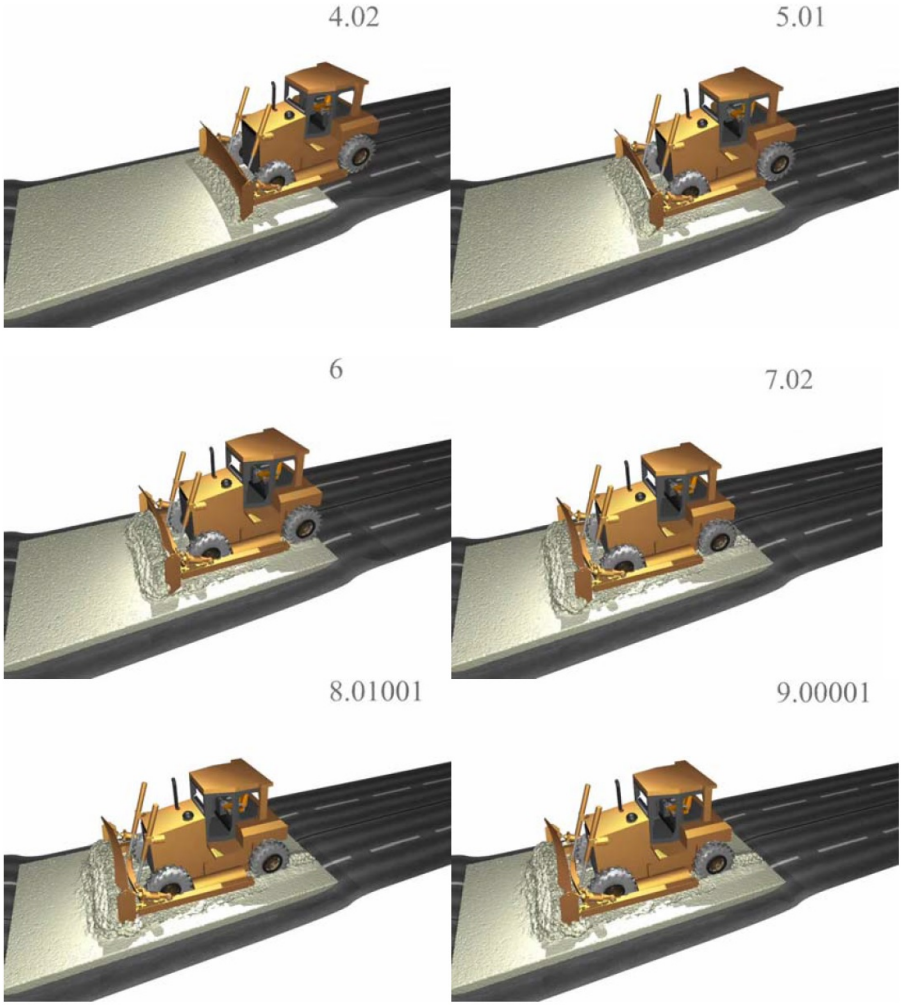

Figure 5.24. Side view snapshots of time 4 to 9 sec of the bulldozer digging soil layer – 5 cm avg. blade penetration, 0 m/s adhesion relaxation speed

www.manaraa.com

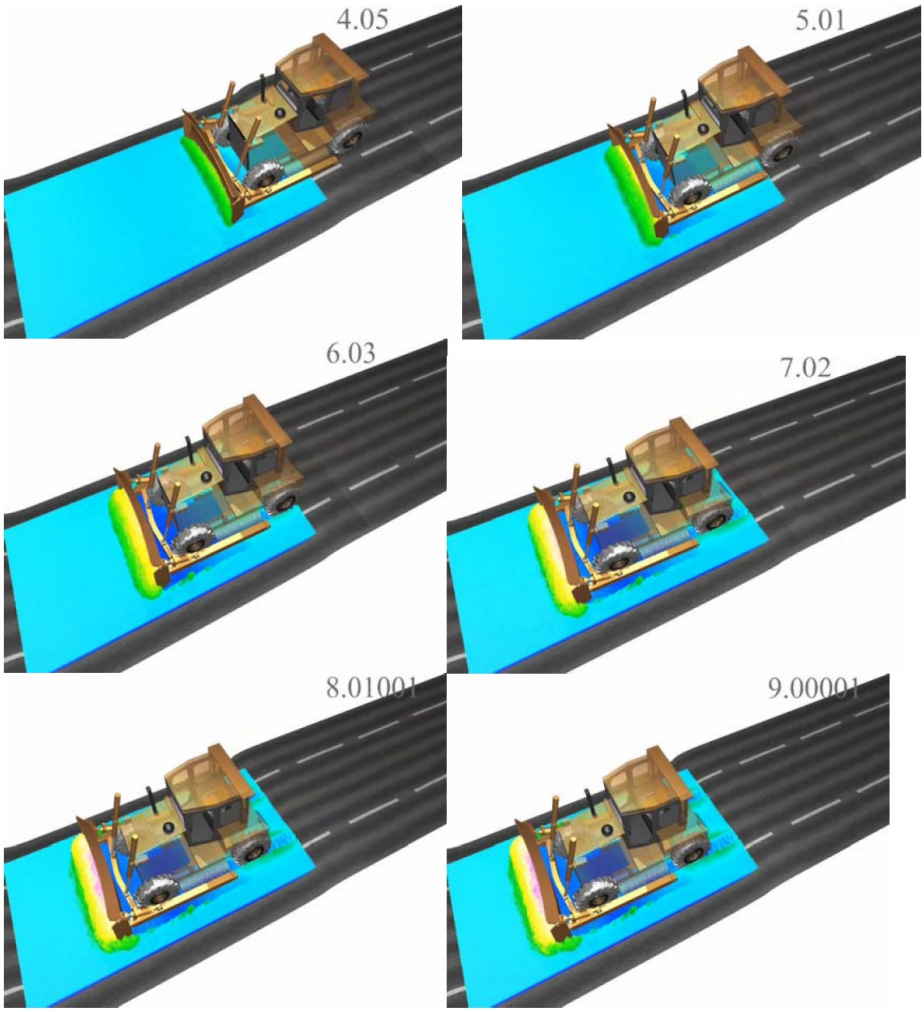

Figure 5.25. Top view snapshots of time 4 to 9 sec of the bulldozer digging soil layer – 5 cm avg. blade penetration, 0 m/s adhesion relaxation speed.

www.manaraa.com

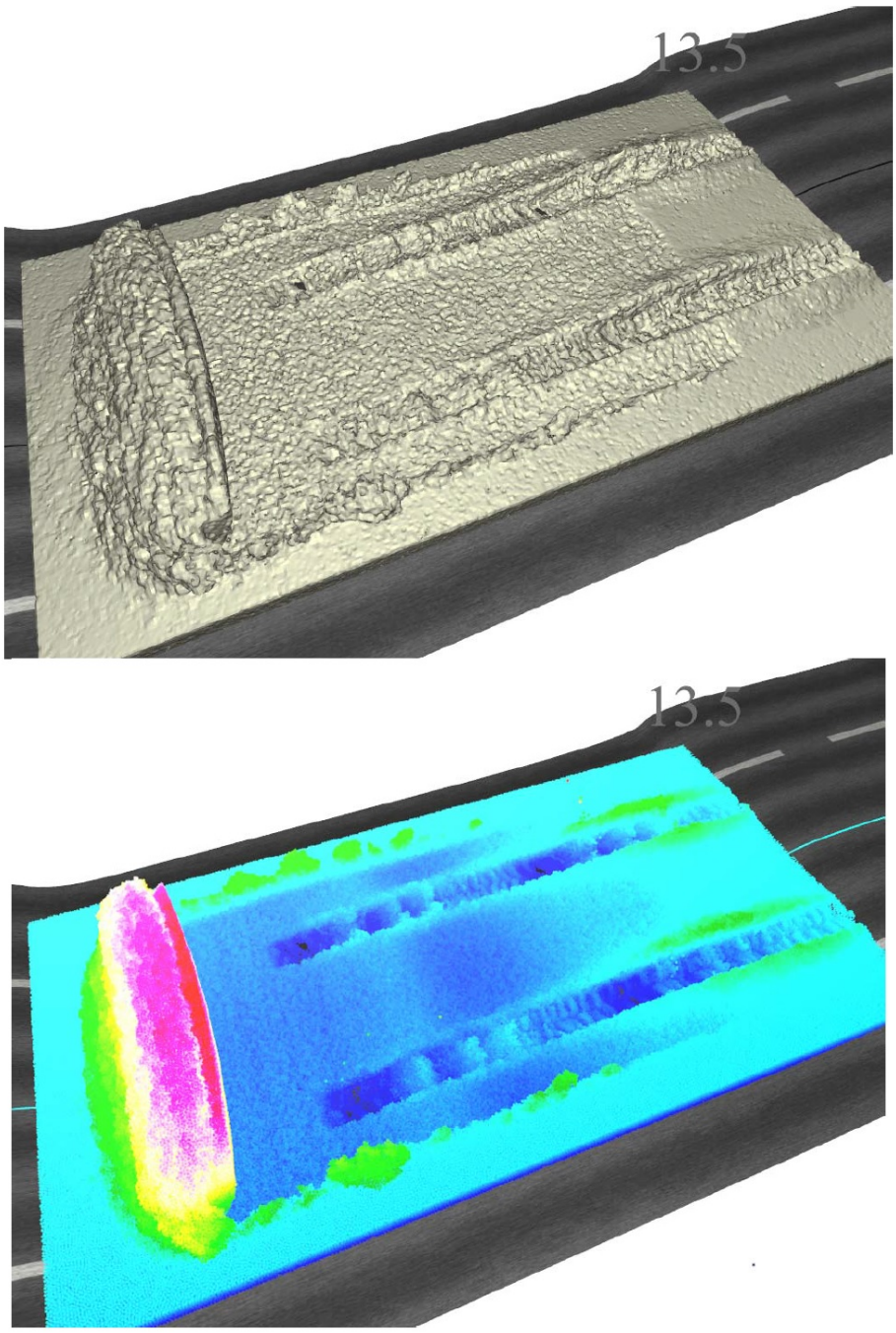

Figure 5.26. Top view snapshots at time 13.5 sec of the bulldozer digging a soil layer – 5 cm avg. blade penetration, 0.0 m/s adhesion relaxation speed.

www.manaraa.com

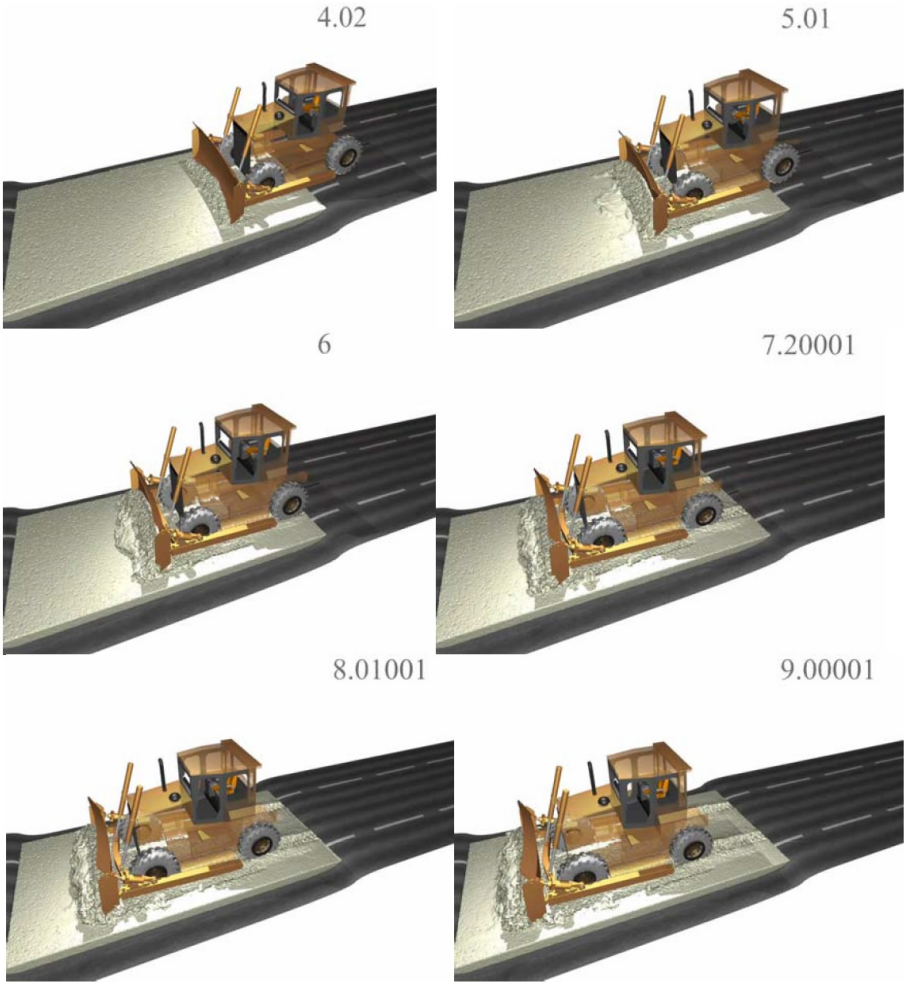

Figure 5.27. Side view snapshots of time 4 to 9 sec of the bulldozer digging soil layer – 5 cm avg. blade penetration, 0.1 m/s adhesion relaxation speed.

www.manaraa.com

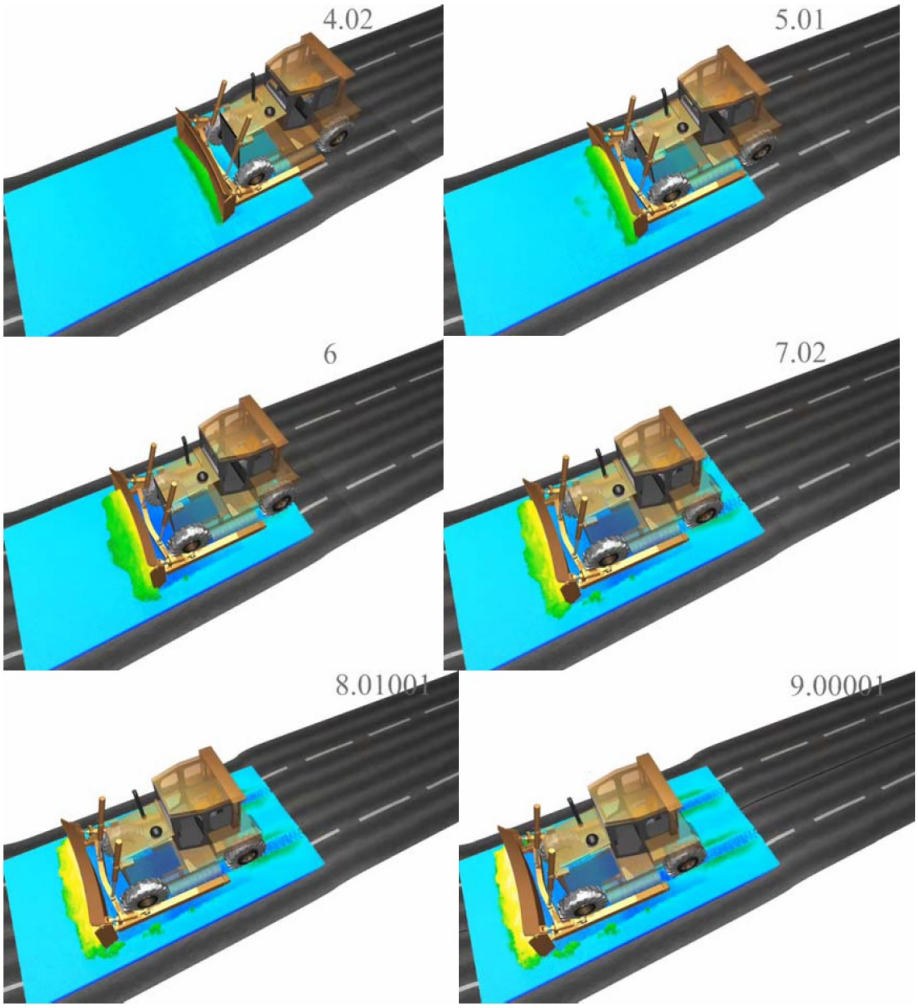

Figure 5.28. Colored elevation view snapshots of time 4 to 9 sec of the bulldozer digging soil layer – 5 cm avg. blade penetration, 0.1 m/s adhesion relaxation speed.

www.manaraa.com

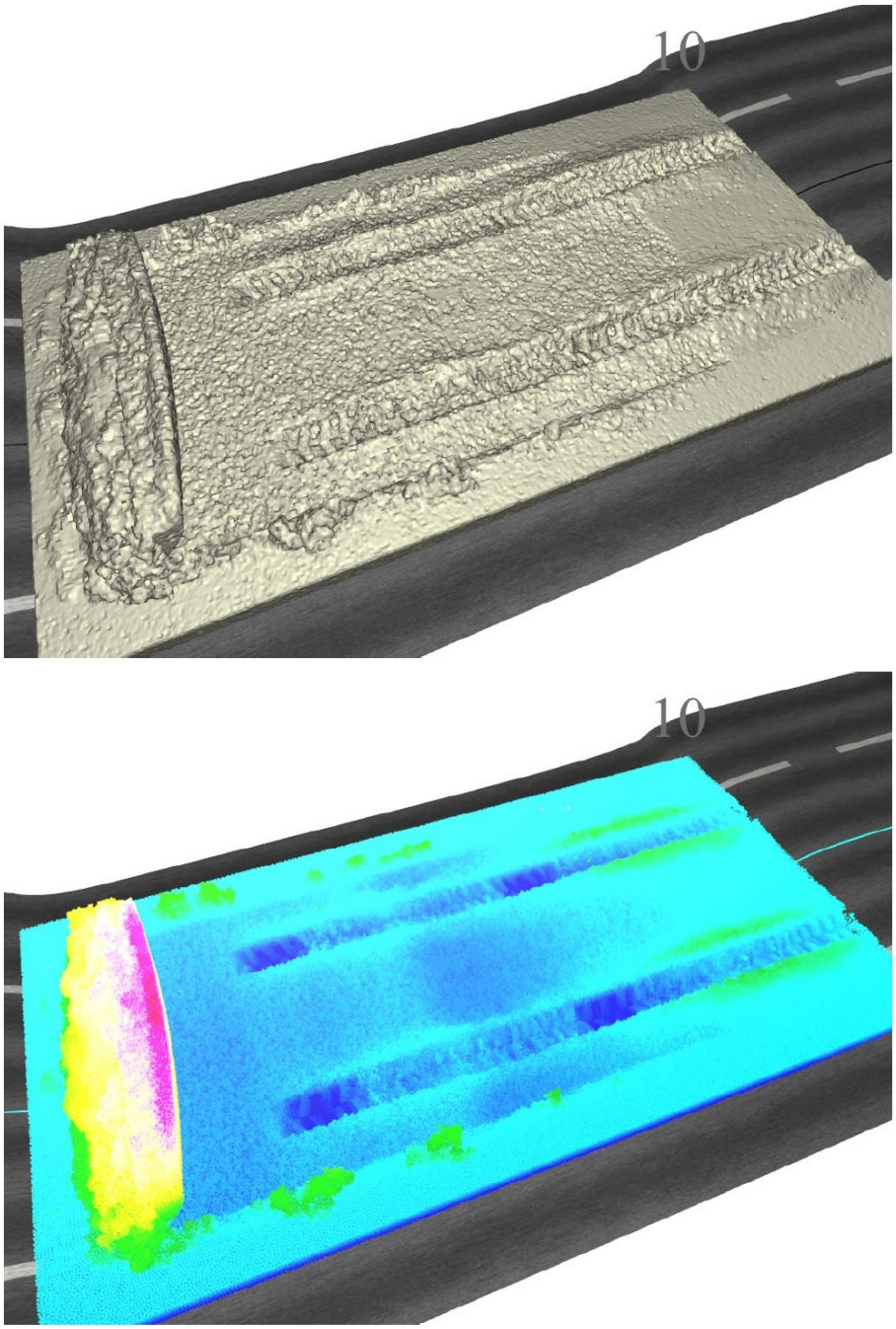

Figure 5.29. Top view snapshots at time 10 sec of the bulldozer digging a soil layer – 5 cm avg. blade penetration, 0.1 m/s adhesion relaxation speed.

www.manaraa.com

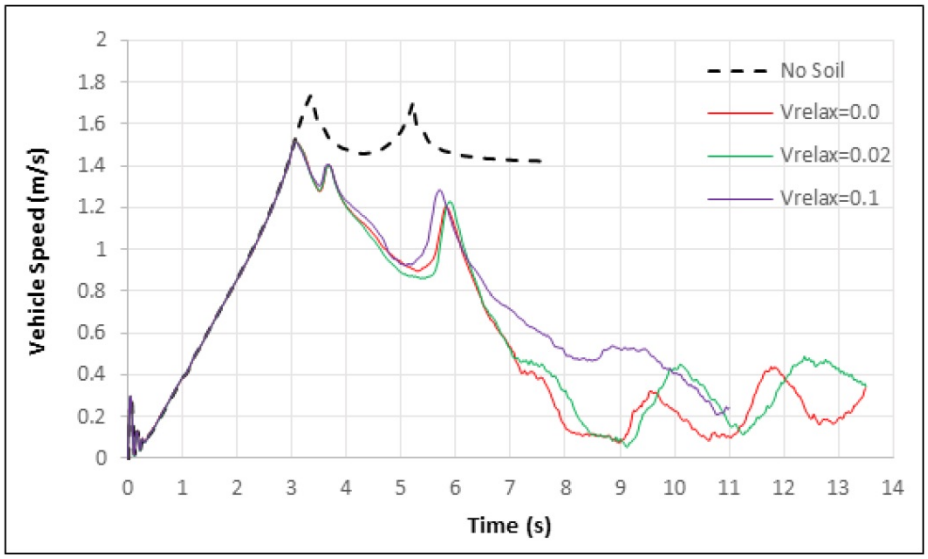

Figure 5.30. Time history of 4-wheel drive bulldozer speed as function of relaxation speed.

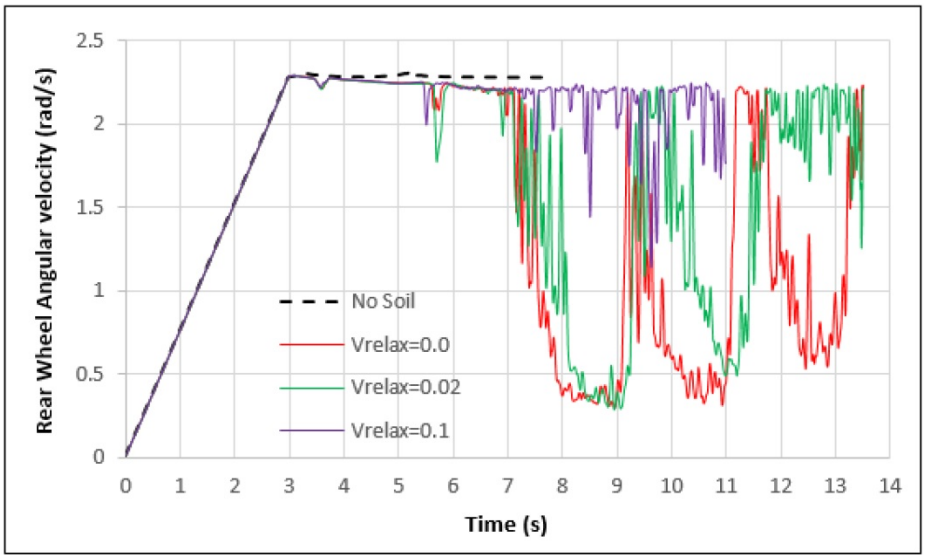

Figure 5.31. Time-history of the angular velocity of the rear wheels for the 4-wheel drive bulldozer as a function of soil relaxation speed.

www.manaraa.com

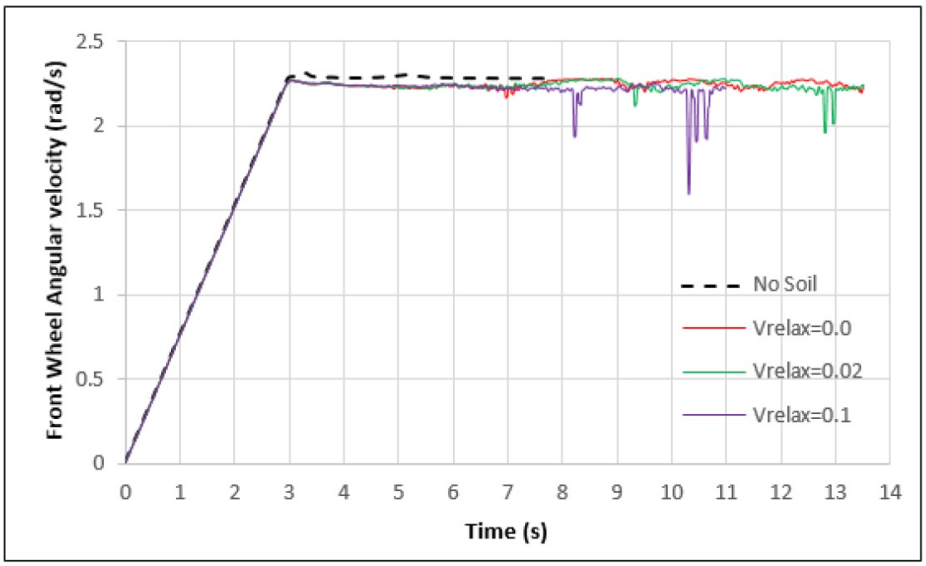

Figure 5.32. Time-history of the angular velocity of the front wheels for the 4-wheel drive bulldozer as a function of soil relaxation speed.

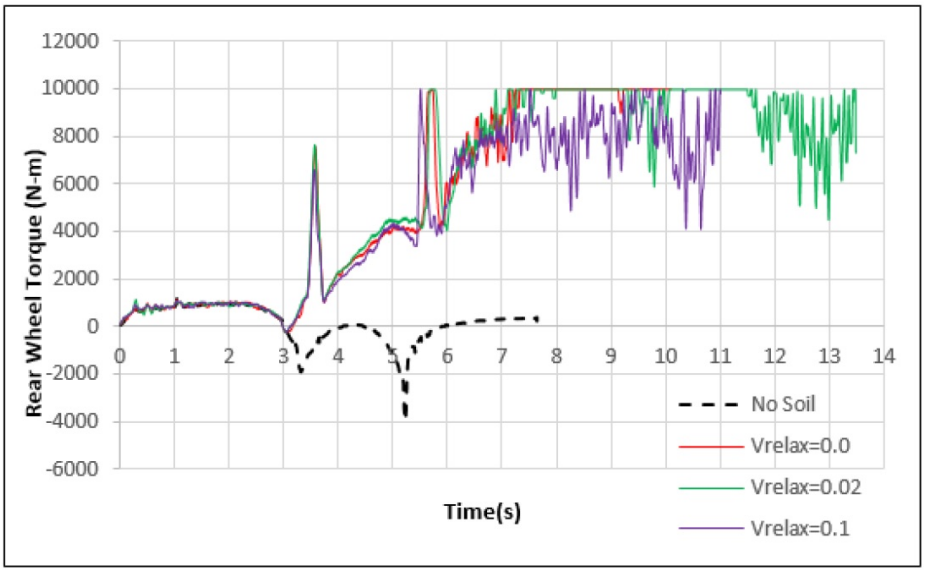

Figure 5.33. Time-history of a rear wheel applied torque for the 4-wheel drive bulldozer as a function of soil relaxation speed.

www.manaraa.com

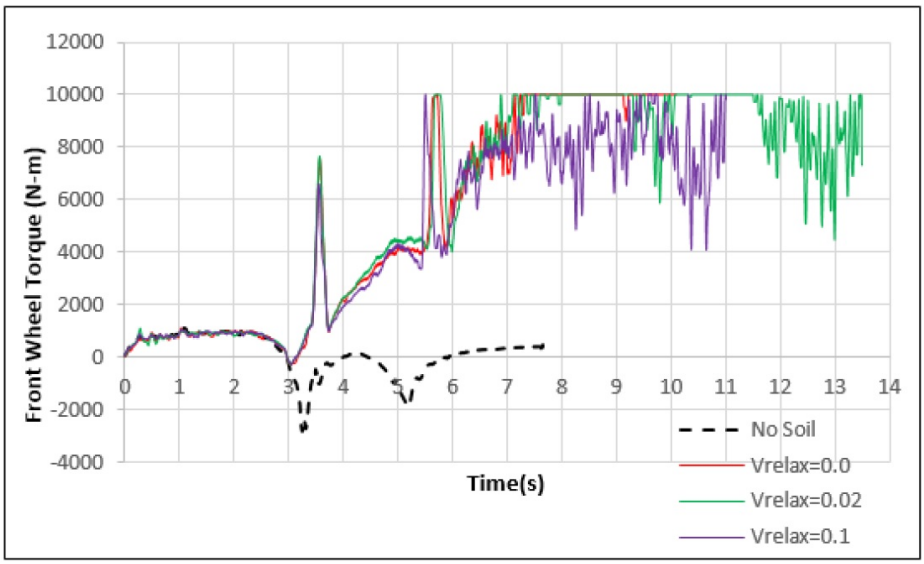

Figure 5.34. Time-history of the front wheels applied torque for the 4-wheel drive bulldozer as a function of soil relaxation speed.

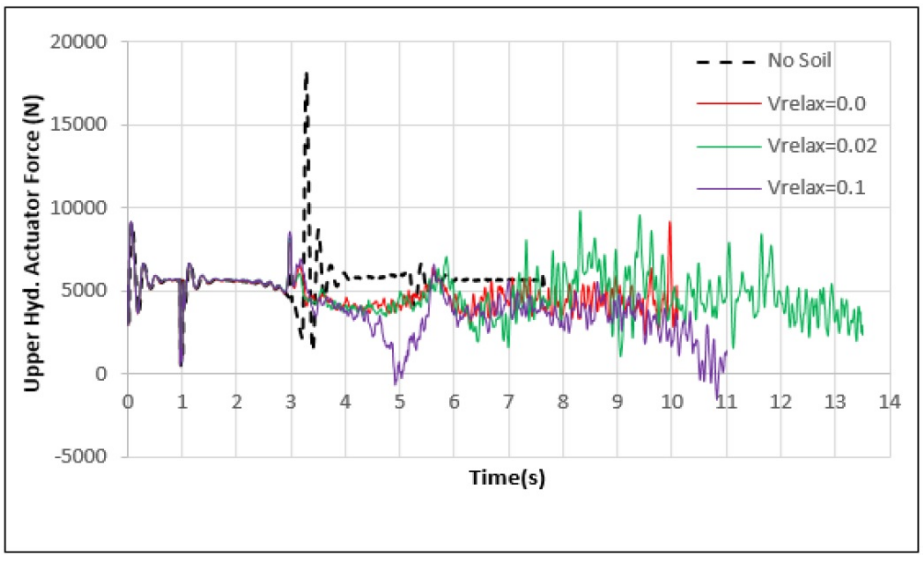

Figure 5.35. Time-history of the upper actuator force for the 4-wheel drive bulldozer as a function of soil relaxation speed.

www.manaraa.com

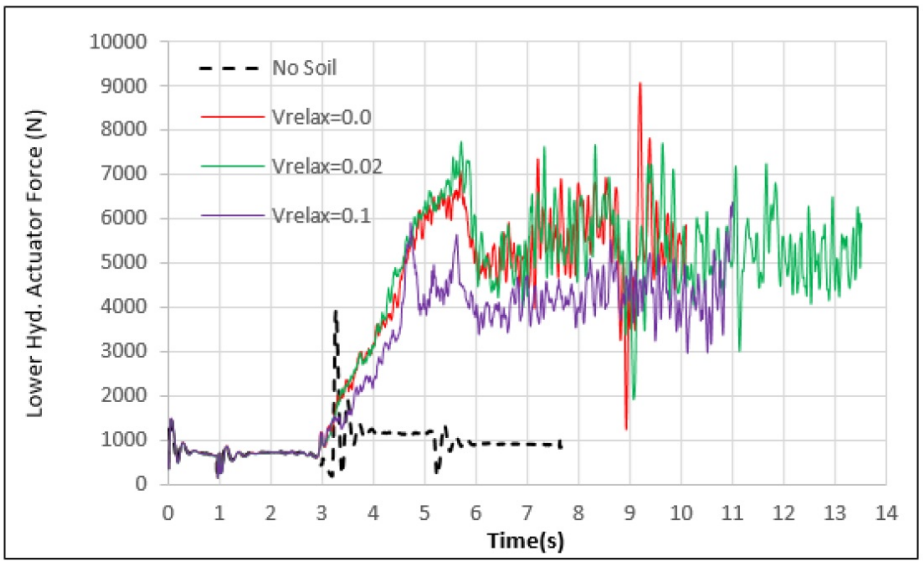

Figure 5.36. Time-history of the lower actuator force for the 4-wheel drive bulldozer as a function of soil relaxation speed.

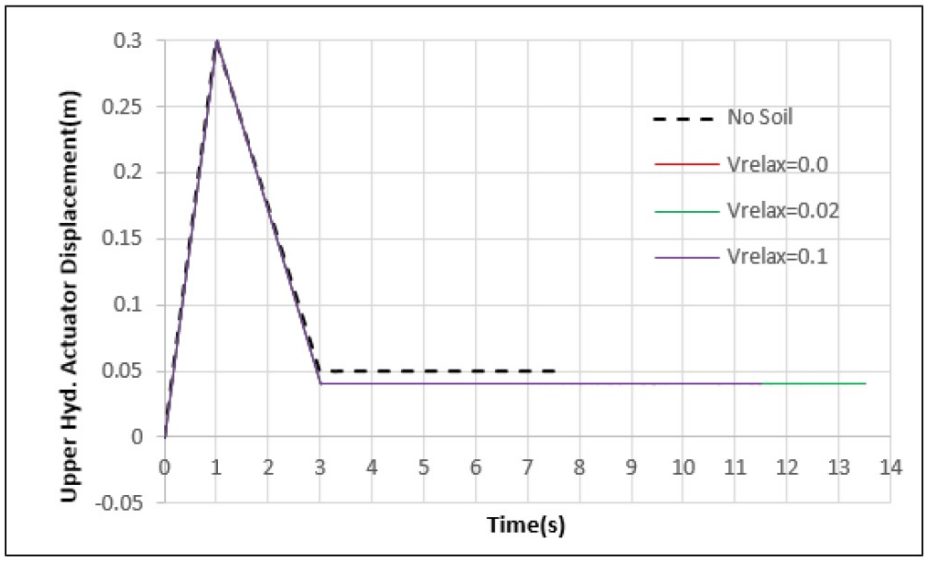

Figure 5.37. Time-history of the upper hydraulic actuator's displacement for the 4-wheel drive bulldozer as a function of penetration depth.

www.manaraa.com

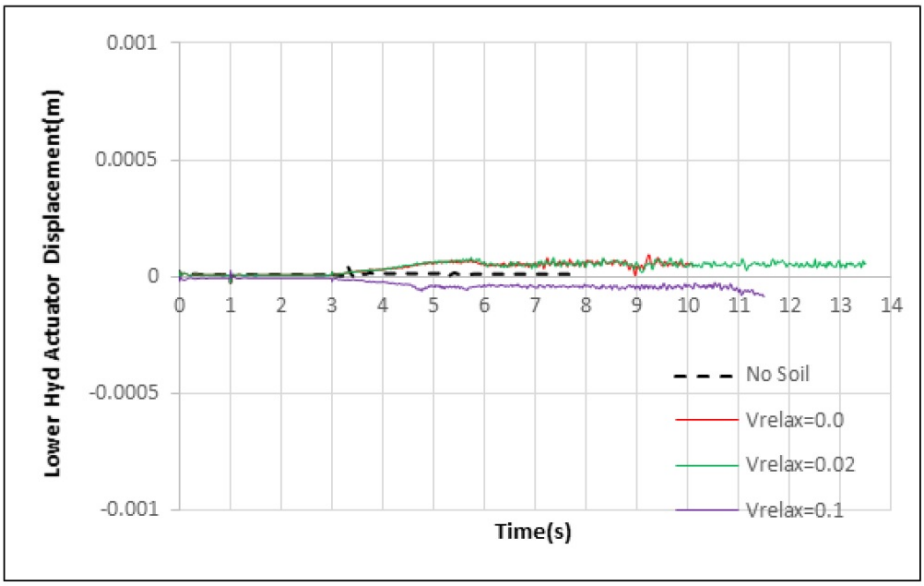

Figure 5.38. Time-history of the lower hydraulic actuator's displacement for the 4-wheel drive bulldozer as a function of penetration depth.

www.manaraa.com

6. CONCLUSIONS AND FUTURE WORK

Multibody dynamics and the discrete element method were integrated into one explicit time integration solver for predicting the dynamic response of a bulldozer excavating and moving through cohesive soft soils (such as mud and snow). Multibody dynamics techniques are used to model the various vehicle components and connect those components using various types of joints and contact surfaces. The model has the following major characteristics:

- A full bulldozer multibody vehicle model is coupled with the DEM particle model using one solver.
- A DEM cohesive soil material model is presented. The model includes the effects of soil compressibility, plasticity, fracture, friction, viscosity, cohesive strength, loss of cohesive strength due to tension and flow. The model parameters can be easily tuned using the main types of soil characterization experiments including: shear cell for measuring the material cohesive strength and piston-cylinder cell for measuring the material bulk density versus consolidating stress.
- A time relaxation sub-model for the soil plastic deformation and cohesive strength is added in order to account for loss in soil cohesive strength and reduced bulk density due to tension or removal of the compression.
- Particle's geometric shape can be modelled using three types of shape representations: superquadric surface, assembly of primitive shapes and a polygonal surface.
- A cartesian eulerian grid contact search algorithm is used to allow fast contact detection between particles.

www.manaraa.com

- The governing equations of motion are solved along with the contact constraint equations using a time-accurate explicit solution procedure.

A numerical simulation of a bulldozer going over a soft soil patch while performing an excavation operation is presented to demonstrate the integrated solver. The solver can be used to predict the excavation performance and mobility of bulldozers and to optimize bulldozer's designs. The model can also be used to predict the performance of other earth moving equipments such as backhoes, loaders and graders.

Some of the immediate future extensions of the work presented in this thesis will include:

- Simulation of bulldozer motion on inclined and tilted slopes.
- Adding a more realistic model to the drive-line of the bulldozer.
- Replacing the wheels with a track and chain drive.

www.manaraa.com

REFERENCES

www.manaraa.com

REFERENCES

[1] W. Schiehlen, "Multibody system dynamics: roots and perspectives," *Multibody system dynamics*, vol. 1, no. 2, pp. 149–188, 1997.

[2] T. M. Wasfy and A. K. Noor, "Computational strategies for flexible multibody systems," *Applied Mechanics Reviews*, vol. 56, no. 6, pp. 553–613, 2003.

[3] T. M. Wasfy and A. Noor, "Modeling and sensitivity analysis of multibody systems using new solid, shell and beam elements," *Computer Methods in Applied Mechanics and Engineering*, vol. 138, no. 1, pp. 187–211, 1996.

[4] T. M. Wasfy, "Modeling spatial rigid multibody systems using an explicit-time integration finite element solver and a penalty formulation," in *ASME 2004 International Design Engineering Technical Conferences and Computers and Information in Engineering Conference*. American Society of Mechanical Engineers, 2004, pp. 901–908.

[5] C. Yildiz and T. M. Wasfy, "Time-accurate multibody dynamics model for toroidal traction drives," in *ASME 2011 International Design Engineering Technical Conferences and Computers and Information in Engineering Conference*. American Society of Mechanical Engineers, 2011, pp. 257–265.

[6] T. M. Wasfy and J. OKins, "Finite element modeling of the dynamic response of tracked vehicles," in *ASME 2009 International Design Engineering Technical Conferences and Computers and Information in Engineering Conference*. American Society of Mechanical Engineers, 2009, pp. 1999–2009.

[7] M. J. Leamy and T. M. Wasfy, "Transient and steady-state dynamic finite element modeling of belt-drives," *Journal of Dynamic Systems, Measurement and Control*, vol. 124, no. 4, pp. 575–581, 2002.

[8] T. M. Wasfy and M. J. Leamy, "Modeling the dynamic frictional contact of tires using an explicit finite element code," in *ASME 2005 International Design Engineering Technical Conferences and Computers and Information in Engineering Conference*. American Society of Mechanical Engineers, 2005, pp. 2381–2388.

[9] T. M. Wasfy, "Asperity spring friction model with application to belt-drives," in *ASME 2003 International Design Engineering Technical Conferences and Computers and Information in Engineering Conference*. American Society of Mechanical Engineers, 2003, pp. 371–378.

[10] T. M. Wasfy and M. J. Leamy, "Modeling the dynamic frictional contact of tires using an explicit finite element code," in *ASME 2005 International Design Engineering Technical Conferences and Computers and Information in Engineering Conference*. American Society of Mechanical Engineers, 2005, pp. 2381–2388.

www.manaraa.com

[11] T. M. Wasfy, "A torsional spring-like beam element for the dynamic analysis of flexible multibody systems," *International Journal for Numerical Methods in Engineering*, vol. 39, no. 7, pp. 1079–1096, 1996.

[12] T. Wasfy, "Lumped-parameters brick element for modeling shell flexible multibody systems," in *18th Biennial Conference on Mechanical Vibration and Noise, ASME International 2001 DETC*, 2001.

[13] T. M. Wasfy, "Edge projected planar rectangular element for modeling flexible multibody systems," in *ASME 2003 International Design Engineering Technical Conferences and Computers and Information in Engineering Conference*. American Society of Mechanical Engineers, 2003, pp. 439–447.

[14] T. Wasfy, "High-fidelity modeling of flexible timing belts using an explicit finite element code," in *ASME 2011 International Design Engineering Technical Conferences and Computers and Information in Engineering Conference*. American Society of Mechanical Engineers, 2011, pp. 1253–1260.

[15] T. M. Wasfy and A. K. Noor, "Object-oriented virtual environment for visualization of flexible multibody systems," *Advances in Engineering Software*, vol. 32, no. 4, pp. 295–315, 2001.

[16] T. M. Wasfy and M. Leamy, "An object-oriented graphical interface for dynamic finite element modeling of belt-drives," in *ASME 2002 International Design Engineering Technical Conferences and Computers and Information in Engineering Conference*. American Society of Mechanical Engineers, 2002, pp. 225–233.

[17] T. Wasfy and M. Leamy, "An object-oriented graphical interface for dynamic finite element modeling of belt-drives," in *ASME 2002 International Design Engineering Technical Conferences and Computers and Information in Engineering Conference*. American Society of Mechanical Engineers, 2002, pp. 225–233.

[18] T. M. Wasfy, "Object-oriented modeling environment for simulating flexible multibody systems and liquid-sloshing," in *ASME 2006 International Design Engineering Technical Conferences and Computers and Information in Engineering Conference*. American Society of Mechanical Engineers, 2006, pp. 831–840.

[19] T. M. Wasfy and H. Wasfy, "Object-oriented environment for dynamic finite element modeling of tires and suspension systems," in *ASME 2006 International Mechanical Engineering Congress and Exposition*. American Society of Mechanical Engineers, 2006, pp. 123–132.

[20] M. Bischoff, E. Onate, D. Owen, E. Ramm *et al.*, "A discrete element model for cohesive soil."

[21] P. Richmond, G. Blaisdell, and C. Green, "Vehicle mobility of wheels and tracks in snow (second validation study of the CRREL shallow snow mobility model). CRREL report 90-13," *US Army Cold Regions Research and Engineering Laboratory, Hanover, NH*, 1990.

[22] P. W. Richmond, S. A. Shoop, and G. L. Blaisdell, "Cold regions mobility models," DTIC Document, Tech. Rep., 1995.

www.manaraa.com

[23] P. W. Haley, M. Jurkat, and P. Brady, "Nato reference mobility model, edition 1 user's guide," in *Technical Report 12503*. US Army Tank-Automotive Command Warren, MI, 1979.

[24] P. Haley, M. Jurkat, and P. Brady, "Nato reference mobility model, edition 1 user's guide," in *Technical Report 12503*. US Army Tank-Automotive Command Warren, MI, 1979.

[25] M. G. Bekker, *Theory of land locomotion*. Ann Arbor, MI: University of Michigan Press, 1956.

[26] M. Bekker, *Introduction to terrain-vehicle systems*. Ann Arbor, MI: University of Michigan Press, 1969.

[27] J. Wong, *Theory of Ground Vehicles*. New York, John Wiley & Sons, 2008.

[28] D. Rubinstein and R. Hitron, "A detailed multi-body model for dynamic simulation of off-road tracked vehicles," *Journal of Terramechanics*, vol. 41, no. 2, pp. 163–173, 2004.

[29] MSC Software, *ADAMS*, (accessed 2014). [Online]. Available: http://www.mscsoftware.com/

[30] FunctionBay, Inc., *RecurDyn/ Solver Theory Manual*, (accessed 2014). [Online]. Available: http://www.functionbay.co.kr/documentation/theoreticalmanual/Theoretical_Manual.pdf

[31] J. Raymond and P. Jayakumar, "Tracked vehicle-soft soil interactions and design sensitivities for path clearing systems utilizing multi-body dynamics simulation methods," DTIC Document, Tech. Rep., 2013.

[32] A. Gibbesch and B. Schafer, "Multibody system modelling and simulation of planetary rover mobility on soft terrain," in *8th International Symposium on Artificial Intelligence, Robotics and Automation in Space (i-SAIRAS 2005), Munich, Germany, September*, 2005, pp. 5–8.

[33] R. Krenn and G. Hirzinger, "SCM - a soil contact model for multi-body system simulations," in *11th European Regional Conference of the International Society for Terrain-Vehicle Systems, Bremen, Germany*, 2009.

[34] R. Krenn and A. Gibbesch, "Soft soil contact modeling technique for multi-body system simulation," in *Trends in Computational Contact Mechanics*. Springer, 2011, pp. 135–155.

[35] SIMPACK, *Multi-Body Simulation Software*, (accessed 2014). [Online]. Available: http://www.simpack.com/

[36] J. Madsen, A. Seidl, D. Negrut, P. Ayers, G. Bozdech, J. Freeman, J. O'Kins, and A. Reid, "A physics based vehicle terrain interaction model for soft soil off-road vehicle simulations," DTIC Document, Tech. Rep., 2012.

[37] Z. Janosi and B. Hanamoto, "Analytical determination of drawbar pull as a function of slip on tracked vehicles in deformable soils, 1st intern," in *Conf. on Terrain-Vehicles Systems, Turin*, 1961.

www.manaraa.com

[38] G. Regli, A. Handke, and M. Bütikofer, "Material laws as a basis for simulation models for the calculation of wheel-soil interaction examination using the finite element method," *Journal of Terramechanics*, vol. 30, no. 3, pp. 165–179, 1993.

[39] S. Shoop, P. Richmond, and J. Lacombe, "Overview of cold regions mobility modeling at CRREL," *Journal of Terramechanics*, vol. 43, no. 1, pp. 1–26, 2006.

[40] M. Tekeste, E. Tollner, R. Raper, T. Way, and C. Johnson, "Non-linear finite element analysis of cone penetration in layered sandy loam soil–considering pre-compression stress state," *Journal of Terramechanics*, vol. 46, no. 5, pp. 229–239, 2009.

[41] K. Xia, "Finite element modeling of tire/terrain interaction: Application to predicting soil compaction and tire mobility," *Journal of Terramechanics*, vol. 48, no. 2, pp. 113–123, 2011.

[42] D. C. Drucker and W. Prager, "Soil mechanics and plastic analysis or limit design," *Quarterly of Applied Mathematics*, vol. 10, 2013.

[43] P. A. Cundall, "A computer model for simulating progressive large scale movements in blocky rock systems," in *Proc. Symp. Rock Fracture (ISRM), Nancy*, vol. 1, 2013.

[44] P. A. Cundall and O. D. Strack, "A discrete numerical model for granular assemblies," *Geotechnique*, vol. 29, no. 1, pp. 47–65, 1979.

[45] A. R. Carrillo, D. A. Horner, J. F. Peters, and J. E. West, "Design of a large scale discrete element soil model for high performance computing systems," in *Proceedings of the 1996 ACM/IEEE conference on Supercomputing*. IEEE Computer Society, 1996, p. 51.

[46] D. A. Horner, J. F. Peters, and A. Carrillo, "Large scale discrete element modeling of vehicle-soil interaction," *Journal of Engineering Mechanics*, vol. 127, no. 10, pp. 1027–1032, 2001.

[47] A. Munjiza, J. F. Peters, M. A. Hopkins, R. Kala, and R. E. Wahl, "A poly-ellipsoid particle for non-spherical discrete element method," *Engineering Computations*, vol. 26, no. 6, pp. 645–657, 2009.

[48] H. Nakashima and A. Oida, "Algorithm and implementation of soil–tire contact analysis code based on dynamic FE–DE method," *Journal of Terramechanics*, vol. 41, no. 2, pp. 127–137, 2004.

[49] W. Smith and H. Peng, "Modeling of wheel–soil interaction over rough terrain using the discrete element method," *Journal of Terramechanics*, vol. 50, no. 5, pp. 277–287, 2013.

[50] D. Negrut, H. Mazhar, D. Melanz, D. Lamb, P. Jayakumar, M. Letherwood, A. Jain, and M. Quadrelli, "Investigating the mobility of light autonomous tracked vehicles using a high performance computing simulation capability," DTIC Document, Tech. Rep., 2012.

[51] D. Negrut, D. Melanz, H. Mazhar, D. Lamb, P. Jayakumar, and M. Letherwood, "Investigating through simulation the mobility of light tracked vehicles operating on discrete granular terrain," SAE Technical Paper, Tech. Rep., 2013.

www.manaraa.com

[52] A. Tasora, M. Anitescu, S. Negrini, and D. Negrut, "A compliant visco-plastic particle contact model based on differential variational inequalities," *International Journal of Non-Linear Mechanics*, vol. 53, pp. 2–12, 2013.

[53] M. Alsaleh, "Soil–machine interaction: Simulation and testing," in *Advances in Bifurcation and Degradation in Geomaterials*. Springer, 2011, pp. 165–176.

[54] S. G. Ahmadi, T. M. Wasfy, H. M. Wasfy, and J. M. Peters, "High-fidelity modeling of a backhoe digging operation using an explicit multibody dynamics code with integrated discrete particle modeling capability," in *ASME 2013 International Design Engineering Technical Conferences and Computers and Information in Engineering Conference*. American Society of Mechanical Engineers, 2013, pp. V07AT10A031–V07AT10A031.

[55] T. M. Wasfy, S. G. Ahmadi, H. M. Wasfy, and J. M. Peters, "Multibody dynamics modeling of sand flow from a hopper and sand angle of repose," in *ASME 2013 International Design Engineering Technical Conference, 9th International Conference on Multibody Systems, Nonlinear Dynamics, and Control (MSNDC), Paper No. DETC2013-12914*, 2013.

[56] T. M. Wasfy, H. M. Wasfy, and J. M. Peters, "Coupled multibody dynamics and discrete element modeling of vehicle mobility on cohesive granular terrains," in *ASME 2014 International Design Engineering Technical Conferences and Computers and Information in Engineering Conference*. American Society of Mechanical Engineers, 2014, pp. V006T10A050–V006T10A050.

[57] R. A. Gingold and J. J. Monaghan, "Smoothed particle hydrodynamics: theory and application to non-spherical stars," *Monthly notices of the royal astronomical society*, vol. 181, no. 3, pp. 375–389, 1977.

[58] J. J. Monaghan, "Smoothed particle hydrodynamics," *Reports on Progress in Physics*, vol. 68, no. 8, p. 1703, 2005.

[59] R. Lescoe, M. El-Gindy, K. Koudela, F. Oijer, M. Trivedi, and I. Johansson, "Tire-soil modeling using finite element analysis and smooth particle hydrodynamics techniques," in *ASME 2010 International Design Engineering Technical Conferences and Computers and Information in Engineering Conference*. American Society of Mechanical Engineers, 2010, pp. 3–18.

[60] R. S. Dhillon, R. Ali, M. El-Gindy, D. Philipps, F. Oijer, and I. Johansson, "Development of truck tire-soil interaction model using fea and sph," SAE Technical Paper, Tech. Rep., 2013.

[61] D. Sulsky, S.-J. Zhou, and H. L. Schreyer, "Application of a particle-in-cell method to solid mechanics," *Computer physics communications*, vol. 87, no. 1, pp. 236–252, 1995.

[62] A. Stomakhin, C. Schroeder, L. Chai, J. Teran, and A. Selle, "A material point method for snow simulation," *ACM Transactions on Graphics (TOG)*, vol. 32, no. 4, p. 102, 2013.

[63] I. K. a. Kafaji, "Formulation of a dynamic material point method (mpm) for geomechanical problems," 2013.

www.manaraa.com

[64] S. R. Idelsohn, E. Oñate, and F. D. Pin, "The particle finite element method: a powerful tool to solve incompressible flows with free-surfaces and breaking waves," *International Journal for Numerical Methods in Engineering*, vol. 61, no. 7, pp. 964–989, 2004.

[65] E. Oñate, M. A. Celigueta, S. R. Idelsohn, F. Salazar, and B. Suárez, "Possibilities of the particle finite element method for fluid–soil–structure interaction problems," *Computational Mechanics*, vol. 48, no. 3, pp. 307–318, 2011.

[66] ESI Group Software, *PAM-CRASH and PAM-SHOCK*, (accessed 2014). [Online]. Available: http://www.esi.com.au/

[67] Advanced Science and Automation Corp, *DIS (Dynamic Interactions Simulator)*, (accessed 2014). [Online]. Available: http://www.ascience.com/ScProducts.htm

[68] T. M. Wasfy, H. M. Wasfy, and J. M. Peters, "High-fidelity multibody dynamics vehicle model coupled with a cohesive soil discrete element model for predicting vehicle mobility," *to appear in the 11th International Conference on Multibody Systems, Nonlinear Dynamics, and Control (MSNDC)*, 2015.

[69] A. Standard, "D6128: Standard test method for shear testing of bulk solids using the jenike shear cell. ASTM international," 2000.

www.manaraa.com